

# Determination of the stellar parameters of C-rich hydrostatic stars from spectro-interferometric observations<sup>\*</sup>

C. Paladini<sup>1</sup>, G. T. van Belle<sup>2</sup>, B. Aringer<sup>3</sup>, J. Hron<sup>1</sup>, P. Reegen<sup>1, \*\*</sup>, C. J. Davis<sup>4</sup>, and T. Lebzelter<sup>1</sup>

<sup>1</sup> Department of Astronomy, University of Vienna, Türkenschanzstrasse 17, 1180 Vienna, Austria  
e-mail: claudia.paladini@univie.ac.at

<sup>2</sup> European Southern Observatory, Karl-Schwarzschild-Str. 2, 85748 Garching bei München, Germany

<sup>3</sup> INAF-OAPD, Vicolo dell'Osservatorio 5, 35122 Padova, Italy

<sup>4</sup> Joint Astronomy Centre, 660 North A'ohōkū Place, University Park, Hilo, Hawaii 96720, USA

Received 18 January 2011 / Accepted 20 May 2011

## ABSTRACT

**Context.** Giant stars, and especially C-rich giants, contribute significantly to the chemical enrichment of galaxies. The determination of precise parameters for these stars is a necessary prerequisite for a proper implementation of this evolutionary phase in the models of galaxies. Infrared interferometry opened new horizons in the study of the stellar parameters of giant stars, and provided new important constraints for the atmospheric and evolutionary models.

**Aims.** We aim to determine which stellar parameters can be constrained by using infrared interferometry and spectroscopy; for C-stars in particular we aim to determine the precision that can be achieved as well as its limitations.

**Methods.** For this purpose we obtained new infrared spectra and combined them with unpublished interferometric measurements for five mildly variable carbon-rich asymptotic giant branch stars. The observations were compared with a large grid of hydrostatic model atmospheres and with new isochrones that include the predictions of the thermally pulsing phase.

**Results.** For the very first time we are able to reproduce spectra in the range between 0.9 and 4  $\mu\text{m}$ , and  $K$  broad band interferometry with hydrostatic model atmospheres. Temperature, mass,  $\log(g)$ , C/O and a reasonable range for the distance were derived for all objects of our study. All our targets have at least one combination of best-fitting parameters that lies in the region of the HR-diagram where C-stars are predicted.

**Conclusions.** We confirm that low-resolution spectroscopy is not sensitive to the mass and  $\log(g)$  determination. For hydrostatic objects the 3  $\mu\text{m}$  feature is very sensitive to temperature variations, therefore it is a very powerful tool for accurate temperature determinations. Interferometry can constrain mass, radius, and  $\log(g)$ , but a distance has to be assumed. The large uncertainty in the distance measurements available for C-rich stars remains a major problem.

**Key words.** stars: AGB and post-AGB – stars: atmospheres – stars: carbon – stars: fundamental parameters – techniques: spectroscopic – techniques: high angular resolution

## 1. Introduction

The basic properties and evolutionary status of a star can be determined knowing its mass, luminosity, radius, and chemical composition. Nowadays we are reaching a point where mass estimates are available not only for binary, but also for single objects (see the recent review by [Aufdenberg et al. 2009](#)). This major advance has been mainly achieved by establishing interferometry as a standard tool for investigating stars ([Wittkowski 2004](#)). The combination of high angular and spectral resolution gives the possibility to study the spatial structure of single stellar objects, which were treated before as point sources only. Red giant stars are very good targets for interferometric investigations because of their extended atmosphere and their brightness in the infrared. These stars are the main contributors to the infrared light and to the chemical enrichment of galaxies. Therefore, an accurate determination of their fundamental parameters is mandatory for a proper implementation in the models of galaxies.

[Wittkowski et al. \(2001\)](#) made a first attempt at deriving the parameters of a sample of asymptotic giant branch (AGB) stars by comparing the spectro-interferometric observations with Kurucz model atmospheres. The uncertainty in parallax and bolometric flux dominate the errors. Recently, [Neilson & Lester \(2008\)](#) determined the fundamental parameters of three M-type stars. They combined infrared interferometry with spectro-photometric observations. The interferometric data were obtained with the VLTI/VINCI instrument and were previously interpreted by using PHOENIX and ATLAS atmospheric models ([Hauschildt et al. 1999](#); [Kurucz 1993](#), respectively) in the work of [Wittkowski et al. \(2004, 2006a,b\)](#). [Neilson & Lester \(2008\)](#) used the new generation of SATLAS models ([Lester & Neilson 2008](#)) for the interpretation of the data: in this way the authors were able not only to determine the fundamental parameters, but also to constrain the atmospheric models they used. The typical approach followed in these works to determine the stellar parameters is: (i) determination of the limb darkened radius by fitting the interferometric observations, the resulting radius is converted into a Rosseland radius; (ii) a linear radius is derived by assuming a distance; (iii) an effective temperature is derived by fitting the SED; (iv) the luminosity is obtained through the radius and

<sup>\*</sup> Appendix A is available in electronic form at <http://www.aanda.org>

<sup>\*\*</sup> Deceased 5 February 2011.

**Table 1.** Target list, available photometry, and variability information.

ID	RA	Dec	<i>J</i>	<i>H</i>	<i>K</i>	<i>L</i>	$f_{[12\mu\text{m}]}$	Var. type	Amplitude	Period
			[mag]	[mag]	[mag]	[mag]	[Jy]			
CR Gem	06:34:23.92	+16:04:30.30	3.36	2.07	1.46	0.88 <sup>a</sup>	39.31	Lb	1.20 <i>B</i>	250
HK Lyr	18:42:50.00	+36:57:30.89	3.23	2.15	1.62	0.99 <sup>b</sup>	22.74	Lb	0.40 <i>V</i> <sup>e</sup>	186 <sup>e</sup>
RV Mon	06:58:21.49	+06:10:01.50	3.06	1.96	1.43	0.85 <sup>c</sup>	31.13	SRb	2.19 <i>B</i>	131
Z Psc	01:16:05.03	+06:10:01.50	2.11	1.10	0.70	0.41 <sup>d</sup>	33.42	SRb	1.30 <i>p</i>	144
DR Ser	18 47 21.02	+05 27 18.60	4.12	2.79	2.08	1.38 <sup>a</sup>	15.9	Lb	0.50 <i>V</i> <sup>f</sup>	196 <sup>f</sup>

**Notes.** The amplitude and the period (unless otherwise stated) are derived from the General Catalogue of Variable Stars (GCVS; Samus+2007–2009). The band used for amplitude of variability measurement is also reported; “*p*” denotes photographic plates. <sup>(a)</sup> Kerschbaum et al. (1996a); <sup>(b)</sup> Kerschbaum et al. (1996b); <sup>(c)</sup> Epchtein et al. (1990); <sup>(d)</sup> Bagnulo (1996); <sup>(e)</sup> Beichman et al. (1988); <sup>(f)</sup> Pojmanski (2002).

$T_{\text{eff}}$ ; (v) the gravity and the mass of the star are constrained by comparison with the theoretical models.

The targets of our study are an important subclass of the AGB objects: the carbon-rich AGB stars. According to theory, only stars with a range of mass between 1 and 4  $M_{\odot}$  undergo the third dredge-up during their AGB phase, with the result of increasing their C/O ratio (Iben & Renzini 1983). The spectra of these giants are consequently dominated by the absorption features of carbonaceous molecular species such as CO, CN, HCN, C<sub>2</sub>, C<sub>3</sub>, and C<sub>2</sub>H<sub>2</sub> (Tsuji 1986; Jørgensen et al. 2000; Loidl et al. 2001). As a result, these objects are the main contributors to the C-enrichment of the ISM.

The state-of-the-art model atmospheres for C-stars are very promising, because they are able to produce large grids of models (Aringer et al. 2009; Mattsson et al. 2010) that describe the observed properties of these objects reasonably well. The hydrostatic model atmospheres for C-stars were compared with optical and infrared spectroscopy in Jørgensen et al. (2000), Loidl et al. (2001), and Abia et al. (2010) and references therein. The major difference between an earlier generation of models as used by Jørgensen et al. (2000), and Loidl et al. (2001), and the hydrostatic atmospheres applied in our work (Aringer et al. 2009) is the inclusion of atomic opacities and an update to new and more accurate molecular opacities.

The stellar evolutionary calculations reached a highly sophisticated level as well, being able to include a detailed thermally pulsing phase with third dredge-up, hot-bottom burning and variable molecular opacity (Marigo et al. 2008).

The purpose of this work is to find out which stellar parameters can be determined for weakly variable C-stars (visual amplitude  $\leq 2$  mag) by using spectroscopy, infrared interferometry, and hydrostatic model atmospheres; and to assess the accuracy. We aim to test the stellar atmospheric models with different techniques and a multiwavelength approach. This is a very important step because errors in the model structure limit quantitative checks of stellar evolution. Our approach in the parameter determination is slightly different from the one adopted by Neilson & Lester (2008) for a few simple reasons: (1) the Rosseland radius is not a direct observable, and in the C-stars (in contrast to M-type AGB stars) there are no windows in the near-infrared where to measure a “continuum” radius (Paladini et al. 2009); (2) it is very rare to obtain simultaneous multiwavelength photometric observations, which is mandatory when dealing with variable stars. Nevertheless, the parameters determined in this work will be compared in a follow-up paper (van Belle et al., in prep.) with that obtained by combining photometric and interferometric observations.

A short description of the acquired observations and of the data reduction for both spectroscopy and interferometry will be

given in Sect. 2. The hydrostatic model atmospheres and the methods for determining the observables will be presented in Sect. 3. The approach used to determine the stellar parameters (temperature, C/O, mass,  $\log(g)$ ) is presented in Sect. 4, while in Sect. 5 we summarise the comparison with the evolutionary tracks. We present a detailed discussion of the single objects studied in this work in Sect. 6, followed by a more general discussion of the obtained results (Sect. 7) and the conclusions (Sect. 8).

## 2. Observations and data reduction

Five mildly variable stars were selected for this investigation: CR Gem, HK Lyr, RV Mon, Z Psc, DR Ser. In Table 1 the coordinates of the objects, near-infrared photometry, and the 12  $\mu\text{m}$  IRAS flux are presented together with period (*P*) and amplitude (*A*) of variability. Unless otherwise stated, *A* and *P* are derived from the General Catalogue of Variable Stars (GCVS; Samus+2007–2009). The amplitude values list the maximum amplitude recorded, and might be based only on few data points, sometimes recorded on photographic plates. More recent observations from the public surveys such as ASAS (Pojmanski 2002) and the Hipparcos Variability Annex (Beichman et al. 1988) show the smaller *V* amplitude variations, often quite stable over a long period. These more recent values are listed in the discussion of the individual targets (Sect. 6). The objects selected are semiregular or irregular variables. The variability amplitude and the period indicate that the atmospheres of our targets can be represented with hydrostatic models. The literature values of *A* and *P* are low compared to dynamic objects such as Mira stars (*P* longer than one year, and *A* of several *V* magnitudes). In the recent grid of dynamic models for C-stars from Mattsson et al. (2010) almost all models with a period lower than 250 days do not develop a stellar wind. The few exceptions are models with extremely low temperature or a very high C/O value. The same applies to the predictions of the previous generations of dynamic models (i.e. Table 1 Gautschy-Loidl et al. 2004). The temperature-density structure of these windless models varies only slightly around the hydrostatic configuration. These small variations of the atmospheric structure are also reflected in the resulting spectra, but as can be seen in Fig. A.1 of Nowotny et al. (2010), the spectra of objects with very mild pulsations and no mass loss do not differ significantly from the corresponding one based on a hydrostatic model. The hydrostatic spherical symmetric approximation will also be checked with interferometric observations (where possible) in Sect. 2.2. We collected for all the targets *IJKL* infrared spectroscopy and *K* broad band interferometric observations.

**Table 2.** Spectral type, photometry, and effective temperature of the standard stars used for the spectroscopic calibration.

ID	Sp. type	$V$ [mag]	$J$ [mag]	$H$ [mag]	$K$ [mag]	$T_{\text{eff}}$ [K]
HIP 92946	A5V	4.62	4.160	4.163	4.085	7880 <sup>a</sup>
HIP 33024	F0V	5.753	5.308	5.232	5.088	7400 <sup>b</sup>
HIP 5544	F0V	5.160	4.764	4.545	4.393	7500 <sup>c</sup>

**Notes.** The photometry is from the 2MASS All Sky catalogue (Cutri et al. 2003); <sup>(a)</sup> Erspamer & North (2003); <sup>(b)</sup> Masana et al. (2006); <sup>(c)</sup> Solano & Fernley (1997).

## 2.1. Spectroscopy

The spectra for our targets were obtained with the UIST instrument (Ramsay et al. 2004) on the United Kingdom InfraRed Telescope (UKIRT) as part of the UKIRT Service Programme: u/serv/1790 and u/serv/1810. The first run of observations was on 29 June 2008; the second one on 20, 23, 25, and 26 January 2009. Four grism spectra were collected for every target, covering the following spectral ranges:  $IJ$  with wavelengths in the interval<sup>1</sup> [0.862, 1.418]  $\mu\text{m}$ ;  $HK$  with wavelengths in the interval [1.395, 2.506]  $\mu\text{m}$ ; short  $L$ , and long  $L$  bands covering [2.905, 3.638] and [3.620, 4.232]  $\mu\text{m}$ , respectively. We also obtained spectra for three standard stars to be used for the calibration procedure. The spectral type, photometry, and effective temperature of the standard stars are listed in Table 2. Because our objects were bright, we observed with a 2-pixel (0.24 arcsec) wide slit. Targets and standard stars were nodded along the slit, with spectra being taken in an A-B-B-A sequence to facilitate first-order sky subtraction. Exposure times of 2-coadds  $\times$  2 s or 1-coadd  $\times$  4 s were used with each grism, depending on the brightness of the source. The nodding sequence was executed twice, resulting in a total integration time of 32 s per source in each grism. The resolution of the spectra ranges between 400 ( $IJ$ ) and 1800 (long  $L$ ). HIP 92946 was used to remove telluric features for targets observed in 2008 (HK Lyr, DR Ser), while HIP 33024 and HIP 5544 were used for the 2009 observations (CR Gem, RV Mon and Z Psc, respectively).

Data reduction was performed using the ORAC-DR UIST pipeline (Cavanagh et al. 2003). The subtraction of the sky removes the OH lines and the thermal background emission. At this stage the spectrum is made of a positive and a negative part, which can be extracted. An Argon lamp is used for the calibration of the object in wavelength. Before every target observation a telluric standard was observed. The observations of target and reference star are always carried out in a range of airmass between 1.0 and 1.3. Only in one case we had airmass 1.5. The airmass difference between target and standard is usually of the order of 0.1, which produces a negligible error in the flux calibration. Once object and standard were calibrated in wavelength, the telluric correction was performed. For this purpose we used the routine IRFLUX from the Starlink<sup>2</sup> software package. IRFLUX divides the standard spectrum by a black body with assigned temperature (the one of the standard). The outcome of this operation is a spectrum that only includes the telluric

<sup>1</sup> Although the wavelengths range of the  $IJ$  grism starts at 0.86  $\mu\text{m}$ , only the part beyond 0.9  $\mu\text{m}$  is usable because the spectral blocking filter blocks emission (essentially has zero transmission) below this wavelength and, in any case, the instrumental throughput drops considerably towards the  $I$  band.

<sup>2</sup> Starlink software is available for downloading on the webpage <http://starlink.jach.hawaii.edu/>.

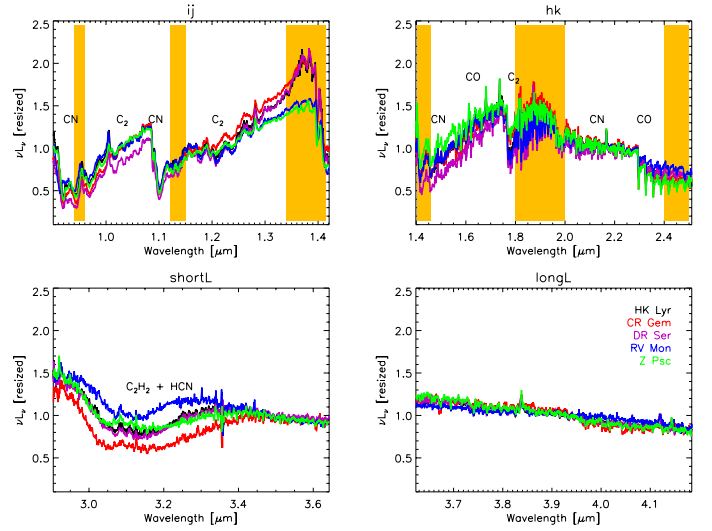


**Fig. 1.** Comparison between all the spectra of our targets. The main molecular features are indicated. The shaded (yellow) regions are affected by absorption of the Earth's atmosphere.

features and atmospheric and instrumental effects. Finally, the target is divided by this last determined spectrum and the telluric calibration is performed. The standard stars are hot enough to be approximated with a black body in the covered wavelength range.

Once the telluric correction was performed, a few emission lines appeared in the spectrum of the targets. Those are the residual of the atmosphere of the standards, which in this part of the spectrum does not contribute to the continuum (this is flat), but it shows few hydrogen lines. We identified those lines by comparing the spectrum of the standards with the corresponding hydrostatic models from Shulyak et al. (2004). The region where the lines are located was not taken into account in the fitting procedure, neither were the data at the edge of the atmospheric windows (shaded region in Fig. 1).

The reddening correction is always a very delicate task in spectroscopy. Every spectrum was dereddened using the EXTIN.PRO IDL procedure (Amôres & Lepine 2005). The code computes the visible extinction ( $A_V$ ) along a path from the Sun to any point in the Galaxy, specified by galactic coordinates and distance. Unfortunately, the distance measurements associated with our objects are very uncertain. We selected three reference distances for each target from the literature: the distance measured by the Hipparcos satellite (Perryman et al. 1997), a distance estimated assuming a constant  $K$  magnitude (Claussen et al. 1987), and a distance estimated by Bergeat & Chevallier (2005), which is based on Hipparcos measurements but takes into account three distinct biases (see Sect. 2.3 of Bergeat et al. 2002). Hereafter, the different distances will be indicated with the abbreviation  $d_{\text{Ber}}$ ,  $d_{\text{Cla}}$ ,  $d_{\text{Hipp}}$ .

The distances for each object are listed in Table 4. The values are in most of the cases very different, but no trend or systematic behaviour can be identified. For the Hipparcos measurements the errors associated to the distances are also given. No error estimation was found in the literature for  $d_{\text{Berg}}$  and  $d_{\text{Cla}}$ , therefore we assume at least 20% of uncertainty. This corresponds to 40% error on the luminosity.

Although the distances have very different values, the resulting reddening correction is very similar (as expected because these are nearby objects). We tested the effect of the different reddening correction on the estimation of the parameters (in

particular the temperature). The typical shift for the temperature determinations is of the order of 10 K, which is low compared to the error bar.

Except for DR Ser, where no correction was applied (see detailed discussion in Sect. 6.5), we used for our computation the reddening correction estimated for the Hipparcos distance.

## 2.2. Interferometry

Observations for this investigation were primarily taken with the Palomar Testbed Interferometer (PTI). The PTI was an 85 to 110 m baselines  $H$  and  $K$  band ( $1.6 \mu\text{m}$  and  $2.2 \mu\text{m}$ ) interferometer located at the Palomar Observatory in San Diego County, California, and is described in detail in Colavita et al. (1999). It had three 40-cm apertures used in pairwise combination for measurements of stellar fringe visibility on sources that range in angular size from 0.05 to 5.0 milliarcsec, being able to resolve individual sources  $\theta > 1.0$  mas in size. The PTI had been in nightly operation since 1997 and was decommissioned in 2009, with minimum downtime during the intervening years. In addition to the carbon stars observed as part of this investigation, appropriate calibration sources were observed as well and can be found in van Belle et al. (2008).

The calibration of the squared visibility ( $V^2$ ) data is performed by estimating the interferometer system visibility ( $V_{\text{SYS}}^2$ ) using the calibration sources with model angular diameters and then normalising the raw carbon star visibility by  $V_{\text{SYS}}^2$  to estimate the  $V^2$  measured by an ideal interferometer at that epoch (Mozurkewich et al. 1991; Boden et al. 1998), (van Belle & van Belle 2005). Uncertainties in the system visibility and the calibrated target visibility are inferred from internal scatter among the data in an observation using standard error-propagation calculations (Boden et al. 1999). Calibrating our point-like calibration objects against each other produced no evidence of systematics, with all objects delivering reduced  $V^2 = 1$ .

The PTI's limiting night-to-night measurement error is  $\sigma_{V_{\text{SYS}}^2} \approx 1.5\text{--}1.8\%$ , the source of which is most likely a combination of effects: uncharacterised atmospheric seeing (in particular, scintillation), detector noise, and other instrumental effects. This measurement error limit is empirically established from the previous study of Boden et al. (1999).

In our sample there is one star, Z Psc, without PTI observations. One visibility measurement taken with IOTA (Infrared Optical Telescope Array) is available in the literature for this object. The visibility point value was obtained in the  $K$ -filter ( $\lambda = 2.2 \mu\text{m}$ ,  $\Delta\lambda = 0.4 \mu\text{m}$ ) and is published in Table 1 of Dyck et al. (1996). We will use this value for our investigation.

Table A.1 gives an overview of the observational parameters of the interferometric observations used, namely UT date, baseline, position angle, and the calibrated visibility with associated error.

From the relationship between visibility and uniform disk (UD) angular size,  $V^2 = [2J_1(x)/x]^2$ , where  $x = \pi B\theta_{\text{UD}}\lambda^{-1}$ , we may establish uniform disk angular sizes for the carbon stars observed by the PTI because the accompanying parameters (projected telescope-to-telescope separation, or baseline,  $B$  and wavelength of observation  $\lambda$ ) are well-characterised during the observation. This uniform disk angular size will be connected to a more physical limb-darkened angular size in Sect. 4. By plotting the UD diameter versus time, we were able to check the reliability of our approximation with hydrostatic models. From the UD diameter versus position angle the assumption of spherical

symmetry is checked. In Fig. 2 we present the interferometric observations for three of our five targets. The missing objects (CR Gem, Z Psc) have only one available measurement. The panels in the first row, identified with the letter “a”, represent the measurements for DR Ser. In the row “b” the points for HK Lyr are plotted, and in the row “c” there are the points for RV Mon. In Col. “1” we present the  $uv$  coverage. In Col. “2” the visibility points are presented versus the baseline. HK Lyr and RV Mon are observed always with the same baseline setup. The variation in the projected baseline is caused by the Earth's rotation. The UD diameter is plotted versus position angle in Col. “3”. In Col. “4” the UD diameter are presented versus the visual phase to investigate eventual variations in the angular size that might be caused among other reason by the pulsation of the stars. The phase estimation for RV Mon and DR Ser is based on the visual light curve from the ASAS database (Pojmanski 2002); while for HK Lyr it is based on the light curve from the Hipparcos Variability Annex (Beichman et al. 1988). Small trends can be identified in the case of RV Mon and HK Lyr, they may be caused by cycle-to-cycle variation, but we can neither completely exclude an instrumental problem (see detailed discussion in Sect. 6.3).

## 3. Hydrostatic models and synthetic observables

For the determination of the parameters we used the new grid of hydrostatic and spherically symmetric model atmospheres of Aringer et al. (2009). They are computed with COMARCS, a programme based on the MARCS code (Gustafsson et al. 1975, 2008) in the version used by Jørgensen et al. (1992) and Aringer et al. (1997). The models are generated assuming hydrostatic local thermal and chemical equilibrium. The molecular and atomic opacity is treated in the opacity sampling (OS) approximation. The parameters that characterise a model are effective temperature, metallicity,  $\log(g)$ , mass, and C/O.

### 3.1. Synthetic spectra

Our observed spectra have higher resolution than those of the grid published in Aringer et al. (2009), therefore new synthetic spectra were computed for a subset of the initial grid of hydrostatic models.

We assumed solar metallicity for our targets. The subset of new spectra covers the following parameters<sup>3</sup>:  $2400 \leq T_{\text{eff}} \leq 4000$  K with steps of 100 K;  $Z/Z_{\odot} = 1$ ;  $-1.0 \leq \log(g[\text{cm s}^{-2}]) \leq +0.0$ ;  $M = 1$  or  $2 M_{\odot}$ ; C/O = 1.05, 1.10, 1.40.

The COMA code (Aringer 2000) was used to compute the opacities for the different layers of a given temperature-density atmospheric structure. The opacity sources included in the calculations for the continuum are listed in Table 1 of Lederer & Aringer (2009). Voigt profiles were used for atomic lines and Doppler profiles for the molecules. All main molecular opacities typical for C-stars were included: CO (Goorvitch & Chackerian 1994),  $\text{C}_2$  (Querci et al. 1974), HCN (Harris et al. 2006), CN (Jørgensen 1997) in the form of line lists, while  $\text{C}_2\text{H}_2$  and  $\text{C}_3$  (Jørgensen et al. 1989) as OS data. This agrees with previous works (Loidl et al. 2001; Aringer et al. 2009; Lederer & Aringer 2009) with the exception of the  $\text{C}_2$  linelist, which was not scaled in the infrared range.

The scaling of the  $gf$  values for  $\text{C}_2$  was suggested for the first time by Jørgensen (1997) and afterwards introduced by Loidl et al. (2001) for fitting spectra of C-rich stars in the range of

<sup>3</sup> In the model grid the lower limit of  $\log(g)$  varies according to the temperature. For more details see Table 1 in Aringer et al. (2009).

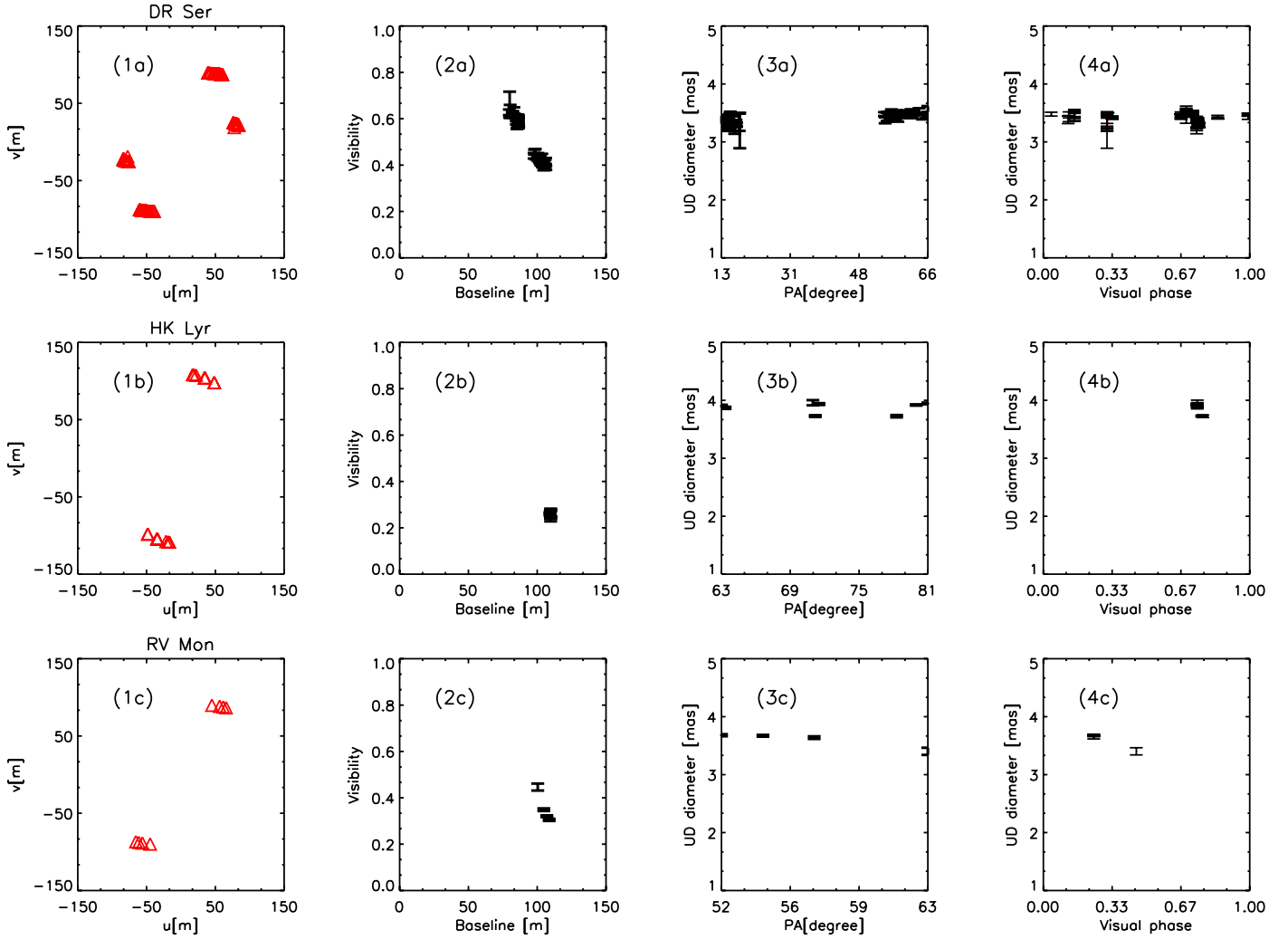


**Fig. 2.** Checking of the hydrostatic and spherical symmetric approximation for the interferometric data. The series of panels “a” refers to DR Ser data, panels “b” to HK Lyr, and panels “c” to RV Mon. The plots in Col. “1” represents the  $uv$ -coverage of the observations, in Col. “2” the visibility points acquired are plotted versus the baselines. In Col. “3” the correspondent UD diameter is plotted versus position angle. In Col. “4” the UD diameter is plotted versus the visual phase.

0.5–2.5  $\mu\text{m}$ . The authors keep the original linelist up to 1.15  $\mu\text{m}$ , they scale it by a factor of 0.1 beyond 1.5  $\mu\text{m}$ , and use a linear extrapolation in the transition region. Different authors already pointed out the need of new  $C_2$  line data. Aringer et al. (2009) showed that the  $C_2$  scaling does not affect the model structure so much, but it introduces a variation in the spectral range between 1.3 and 2.1  $\mu\text{m}$ . In the same work a discrepancy was observed when comparing synthetic and observed ( $H - K$ ) colours. This discrepancy was investigated in terms of  $C_2$  opacity. The authors show in their Fig. 15 how the photometry obtained for unscaled models better agrees with observations. Aringer et al. (2009) conclude that this could be an indication that the use of the linelist in its original version is more appropriate, as long as there are no other more precise sources available.

In order to check this conclusion further, we performed the  $\chi^2$  test as explained in García-Hernández et al. (2007) and Uttenthaler & Lebzelter (2010). In most of the cases we obtained a lower result of the  $\chi^2$  test for the  $C_2$ -unscaled linelist of Querci et al. (1974). This result was also judged by eye in order to test the method. In Fig. 3 the effect of the  $C_2$ -scaling in the  $HK$ -band is shown. The full line is the spectrum of the star Z Psc (upper panel) and HK Lyr (lower panel) convolved to a resolution of 200. The dotted line is the synthetic spectrum corresponding

to a model with scaled  $C_2$  opacity, while the dashed line is the same model with the original  $C_2$  list. The result of the  $\chi^2$  test, the check by eye and the arguments of previous work of Aringer et al. (2009) led us to opt for the original  $C_2$ -unscaled linelist.

The resulting opacities are used as input for a spherically symmetric radiative transfer code that gives the synthetic spectra with a resolution of 18 000 in the wavelength range 0.8–25  $\mu\text{m}$ . We convolved these spectra to obtain same resolution as the observed data.

### 3.2. Synthetic visibility profiles

The spherical radiative transfer code produces an additional output besides the total spectrum: a monochromatic spatial intensity profile. Synthetic visibility profiles for the  $K$ -broad band PTI setup were computed for a subset of the grid of hydrostatic models. The metallicity, the temperature range and the  $C/O$  ratio were fixed (more details in Sect. 4.1). To compute the visibility profiles, i.e. the interferometric observables, we proceeded as follows.

We defined a set of narrow-band filters centred on the sampled wavelength of the transfer function for the PTI  $K$ -broad

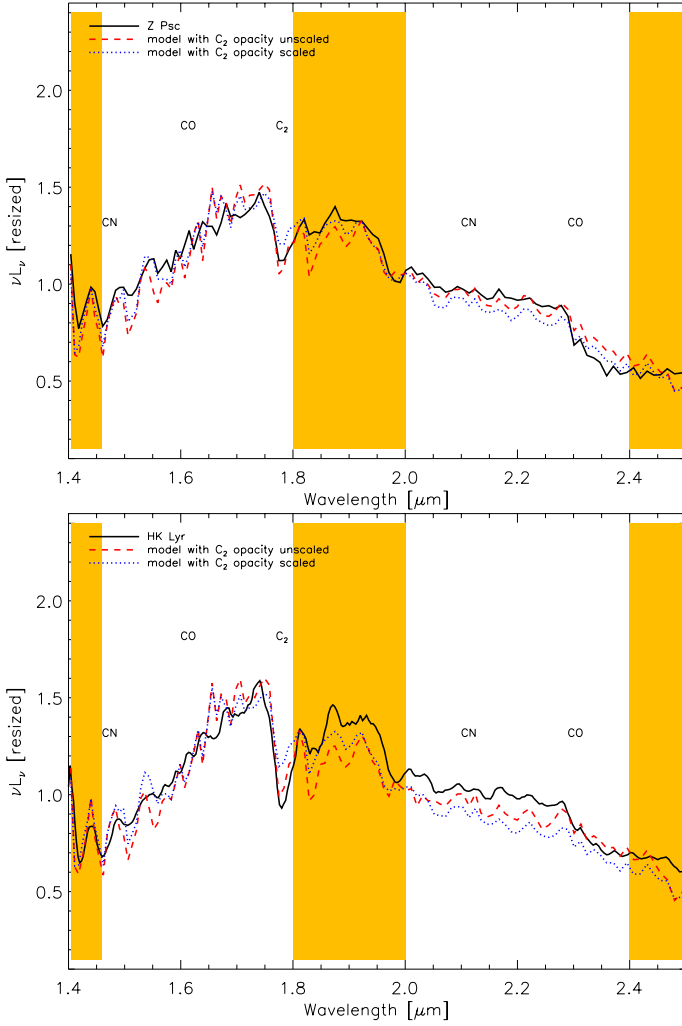


**Fig. 3.** Comparison between the observed spectrum of two targets (black full line, Z Psc in the upper panel and HK Lyr in the lower), a spectrum computed assuming scaled  $C_2$  opacity (dotted line) and the spectrum with unscaled  $C_2$  (dashed line). Shaded bands mark regions of poor atmospheric transmission.

band setup. Then the monochromatic intensity profiles were convolved with the filters so defined. The visibility profiles were computed as Hankel transform of the narrow-band intensity profiles. The spatial frequencies were converted from  $AU^{-1}$  to baselines in meters for a given distance. The squared visibility broad band profile finally is obtained as

$$V_{\text{broad}}^2 = \frac{\sum_i (S_i^2 F_i^2 V_i^2)}{\sum_i (S_i^2 F_i^2)}, \quad (1)$$

were the sum was calculated over the “ $i$ ” narrow band filters;  $S_i$  is the transfer function of PTI in the  $K$  broad band setup;  $F_i$  is the flux integrated over the narrow band filter, and finally  $V_i$  is the visibility corresponding to the narrow band filters. Following this approach for the computation of the broad band visibility profile, the bandwidth smearing effect is properly taken into account (Kervella et al. 2003; Verhoelst 2005; Paladini et al. 2009).

#### 4. Parameter determination

All spectra of the targets appear to be very similar (Fig. 1). They are dominated by the CN,  $C_2$  and CO bands between 0.9 and

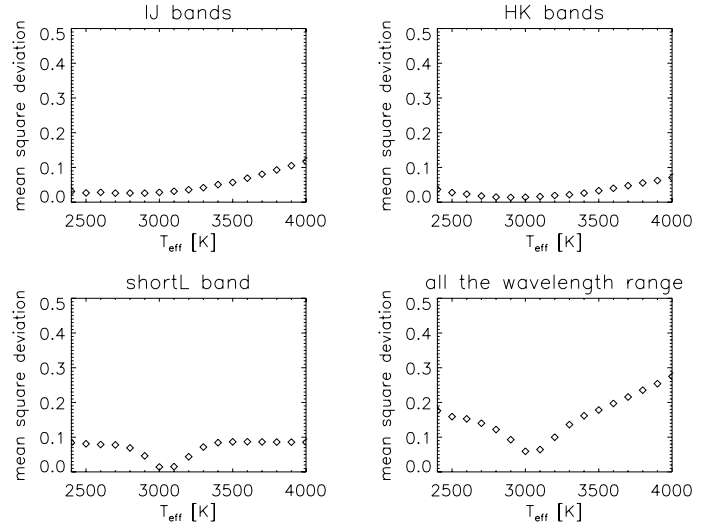


**Fig. 4.** Four plots show the mean squared deviation obtained by fitting single portions of the spectra ( $IJ$ ,  $HK$ , short  $L$ ), and by fitting all the portions of spectra at once (all the wavelength range) for HK Lyr. These plots demonstrate the accuracy of the short  $L$  measurement.

$2.5 \mu\text{m}$ , while the main absorption feature at  $3 \mu\text{m}$  in the  $L$ -band is due to HCN and  $C_2H_2$ . In Fig. 1 the regions affected by telluric absorption are shaded. These regions were of course not considered in our fitting procedure. Loidl et al. (2001) computed the flux ratio of various hydrostatic models (e.g. Fig. 3 of their paper) to investigate the effect of changes in the stellar parameters. They demonstrated that spectral features are mainly sensitive to  $T_{\text{eff}}$  and  $C/O$ . Moreover, Aringer et al. (2009) showed that the synthetic spectrum below  $2.5 \mu\text{m}$  of stars with  $T_{\text{eff}} \geq 3000$  K mildly changes for different values of  $\log(g)$  and mass.

Therefore, we determined  $T_{\text{eff}}$  and  $C/O$  from spectroscopy and turn to the PTI interferometric observations to determine the remaining characteristic parameters of the models: mass and  $\log(g)$ .

##### 4.1. Temperature and $C/O$ ratio

The ratio between the  $3 \mu\text{m}$  ( $C_2H_2$ ) and the  $5.1 \mu\text{m}$  ( $C_3$ ) features is the most powerful tool for determining temperature and  $C/O$  ratio for hydrostatic C-stars (Jørgensen et al. 2000). Unfortunately, our spectral coverage does not reach the  $C_3$  feature at  $5.1 \mu\text{m}$ .

Following the approach of Loidl et al. (2001), we used the energy distribution of the available spectra as main temperature indicator. The observed spectrum was convolved to a lower resolution of  $R = 200$ . Every target of our list was compared with a grid of synthetic spectra with the same resolution. The grid of models is dense enough in temperature to allow an accurate statistic approach, which is described in detail in Appendix A. The  $T_{\text{eff}}$  value was separately estimated for every wavelength range, except for the long  $L$  band. This range of the spectrum is mostly flat and free from features, therefore not very sensitive for the temperature estimation. We also computed a temperature taking into account all four parts of the spectrum. The resulting temperatures are presented in Table 3. Figure 4 shows the mean-squares deviation<sup>4</sup> derived by first fitting single pieces of the spectrum (“ $IJ$ ”, “ $HK$ ”, “short  $L$ ”) and then by fitting all

<sup>4</sup> One root mean square value (rms) was derived by fitting each model. The models were divided into bins of temperature; the single rms values were squared (mean square deviation) to be summed to obtain one value

**Table 3.** Summary of temperature, C/O determination, and rms values corresponding to the different C/O.

ID	$T_{\text{eff}}(IJ)$ [K]	$T_{\text{eff}}(HK)$ [K]	$T_{\text{eff}}(\text{short}L)$ [K]	$T_{\text{eff}}(\text{all spec})$ [K]	rms <sub>1.05</sub>	rms <sub>1.10</sub>	rms <sub>1.40</sub>
CR Gem	2700 ± 200	2860 ± 200	<b>3070 ± 50</b>	2920 ± 190	<b>0.021</b>	0.027	0.038
HK Lyr	2740 ± 220	2920 ± 210	<b>3090 ± 50</b>	3080 ± 120	0.015	0.016	<b>0.013</b>
RV Mon	2950 ± 300	2930 ± 230	<b>3170 ± 50</b>	3210 ± 140	<b>0.006</b>	0.008	0.009
Z Psc	3000 ± 330	3080 ± 210	<b>3130 ± 60</b>	3170 ± 130	<b>0.014</b>	0.017	0.016
DR Ser <sub>no redd correct</sub>	2790 ± 250	2820 ± 200	<b>3080 ± 40</b>	3030 ± 170	<b>0.011</b>	0.013	0.014

**Notes.** The boldface corresponds to the best values of temperature and C/O. More details in Sect. 4.1.

pieces of the spectrum at once (“the entire wavelength range”) for HK Lyr. Our intention is to look for possible minima in the temperature distribution.

The temperature values obtained from the different ranges of wavelength show a trend: by using the *IJH* bands as indicators, cooler temperatures are obtained. This trend can hardly be explained with problems during the calibration. The data reduction procedure (see Sect. 2.1) was accurate enough that we do not expect systematic errors in the overall flux distribution, which are large enough to explain the systematic variations in the temperature. The temperature difference might be explained as the effect of an optically thin dust shell surrounding the star. The effect of a dusty shell on the energy distribution of a star is shown in Figs. 3 and 4 of Nowotny et al. (2011). The model used for this simulation corresponds to a very dynamic star. Our objects are fairly static, but we speculate that a thin dust shell would affect the spectrum in the same way with scaled-down intensity. This shell would absorb the light in the *IJH* band and emit it at longer wavelength. As a direct consequence, a temperature determination based on *IJH* band is systematically lower, as can be seen in the upper panels of Fig. 4. If the shell is thin enough, the effect on the short edge of the *L* band is negligible. This makes the short *L* band temperature determination quite robust, as can be seen in the lower left panel of Fig. 4.

We note that this is not the case if the star is a strongly pulsating variable (such as a Mira). In this case the profile of the 3  $\mu\text{m}$  feature, which is the result of the superposition of molecular opacity and dust continuous emission (Gautschy-Loidl et al. 2004), will be sensitive to the dynamic processes of the atmosphere. The respective temperature derived for every star by fitting the short *L* band will be assumed below.

The second quantity that mainly modifies the appearance of a C-rich spectrum is the C/O ratio. Unfortunately, the relatively low resolution of the spectra available limits the precision of this measurement. The CO band at 2.29  $\mu\text{m}$ , the C<sub>2</sub> bands at 1.02 and 1.20  $\mu\text{m}$ , and the C<sub>2</sub>H<sub>2</sub>+HCN at 3  $\mu\text{m}$  were considered as indicators for the C/O ratio. Following to Loidl et al. (2001), the C<sub>2</sub> features longward of 1.20  $\mu\text{m}$  were not used because of the uncertainty in the C<sub>2</sub> opacity. Two reference wavelengths were chosen to indicate start and end of every selected band. In low-resolution spectroscopy no continuum window is available for C-stars (Paladini et al. 2009), therefore a *pseudo-continuum* was obtained by linear interpolation of the points at the edge of the chosen band. The selected portion of spectrum was normalised to this pseudocontinuum. Following this approach, we derived the equivalent width for the observed spectrum and for all models with the temperature determined from the previous step. Grouping the models in sets according to the C/O (i.e. every

for every bin. The number of models in every bin is not constant, therefore, the final mean-squares deviation was normalised by the number of models in every bin.

“C/O group” includes models with same temperature, but different  $\log(g)$  and mass), a root mean-squares value was obtained for every C/O by comparing the observed equivalent width and the synthetic one.

In Cols. 6–8 of Table 3 the resulting rms for the three C/O values (1.05, 1.10, and 1.40) is given. The minimum rms is shown in bold. All stars of the sample have a low value of C/O ratio, which corresponds to 1.05, except for HK Lyr, where the C/O = 1.4.

#### 4.2. Mass, $\log(g)$ , and distance

As already pointed out by other authors, it is hard to detect the effect of mass and  $\log(g)$  from low-resolution spectroscopy of C-rich stars. This is confirmed in our series of plots in Figs. 6–10, where models with the same parameters except mass and  $\log(g)$  are compared with the spectra of the targets. The temperature and C/O ratio of the models were determined following the procedure described above.

Owing to these considerations, we decided to treat the observables of interferometry as completely independent quantities. Because interferometry aims to measure the radius of the target, the distance becomes an important parameter. Unfortunately, the distance measurements available for these objects are quite imprecise (typical error of the order of 20%) and often contradict each other with differences between measurement relative to the same objects that are larger than errors. The problem we face is degenerate because we have to deal with radius, distance, mass, and all these quantities are related to each other.

We handled the problem in the following way. Three distances obtained with different methods were chosen from the literature for every object (see Sect. 2.1 and Table 4), and a set of synthetic visibility profiles was scaled to every distance. The set has a fixed temperature and C/O ratio. We obtained for every distance the combination of stellar parameters ( $M$ ,  $\log(g)$ ) from the best-fitting profile.

### 5. Comparison with evolutionary tracks

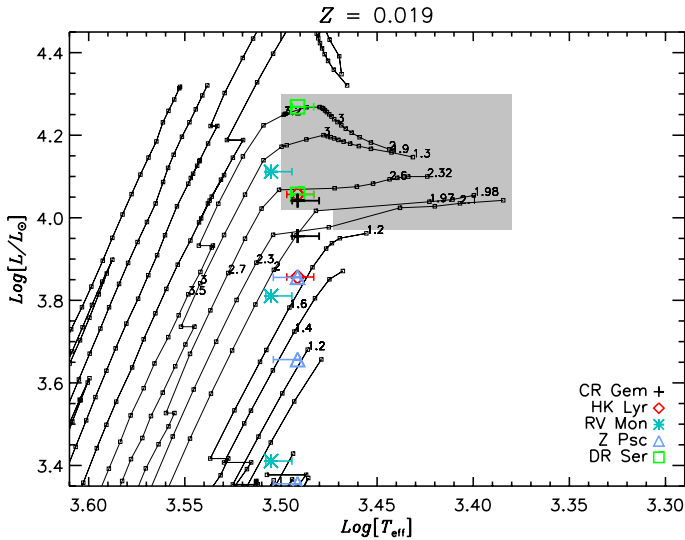
At this point of our investigation, we have one combination of stellar parameters for every object and every distance. To constrain the choice of the parameters even more, we compare them with the recent isochrones for thermally pulsing AGB stars from Marigo et al. (2008). The selection of the isochrones follows the same criteria as Marigo et al. (2008): ages  $\log(t/\text{yr})$  between 7.8 and 10.2, and the spacing in  $\log(t)$  is 0.1 dex.

Figure 5 shows a zoom into the region of the H-R diagram where AGB stars are located. The shaded area identify the region where C-stars are expected. Owing to the discrete sampling of the points in the isochrones (small square), the transition region from M- to C-stars is not very well defined. According to

**Table 4.** Distance measurements and stellar parameters of the model that best fits spectroscopic and interferometric measurements.

Distance	CR Gem	HK Lyr	RV Mon	Z Psc	DR Ser
$d_{\text{Berg}}$	920 pc $L = 11\,000 L_{\odot}$ $T_{\text{eff}} = 3\,100\text{ K}$ C/O = 1.05 $M = 2 M_{\odot}$ $\log(g) = -0.40$	<b>730 pc</b> $L = 7\,186 L_{\odot}$ $T_{\text{eff}} = 3\,100\text{ K}$ C/O = 1.4 $M = 2 M_{\odot}$ $\log(g) = -0.20$	<b>670 pc</b> $L = 6\,400 L_{\odot}$ $T_{\text{eff}} = 3\,200\text{ K}$ C/O = 1.05 $M = 1 M_{\odot}$ $\log(g) = -0.40$	465 pc $L = 4\,534 L_{\odot}$ $T_{\text{eff}} = 3\,100\text{ K}$ C/O = 1.05 $M = 2 M_{\odot}$ $\log(g) = +0.0$	1295 pc $L = 18\,050 L_{\odot}$ $T_{\text{eff}} = 3\,100\text{ K}$ C/O = 1.05 $M = 2 M_{\odot}$ $\log(g) = -0.60$
$d_{\text{Clau}}$	<b>780 pc</b> $L = 9\,025 L_{\odot}$ $T_{\text{eff}} = 3\,100\text{ K}$ C/O = 1.05 $M = 1 M_{\odot}$ $\log(g) = -0.60$	<b>900 pc</b> $L = 11\,389 L_{\odot}$ $T_{\text{eff}} = 3\,100\text{ K}$ C/O = 1.40 $M = 2 M_{\odot}$ $\log(g) = -0.40$	<b>1000 pc</b> $L = 12\,932 L_{\odot}$ $T_{\text{eff}} = 3\,200\text{ K}$ C/O = 1.05 $M = 2 M_{\odot}$ $\log(g) = -0.40$	<b>600 pc</b> $L = 7\,170 L_{\odot}$ $T_{\text{eff}} = 3\,100\text{ K}$ C/O = 1.05 $M = 1 M_{\odot}$ $\log(g) = -0.50$	<b>990 pc</b> $L = 11\,390 L_{\odot}$ $T_{\text{eff}} = 3\,100\text{ K}$ C/O = 1.05 $M = 2 M_{\odot}$ $\log(g) = -0.40$
$d_{\text{Hipp}}$	$323^{+357}_{-111}$ pc - -	$1\,369^{+671}_{-NN}$ pc - -	$450^{+369}_{-140}$ pc $L = 2\,574 L_{\odot}$ $T_{\text{eff}} = 3\,200\text{ K}$ C/O = 1.05 $M = 1 M_{\odot}$ $\log(g) = +0.0$	$323^{+119}_{-68}$ pc $L = 2\,267 L_{\odot}$ $T_{\text{eff}} = 3\,100\text{ K}$ C/O = 1.05 $M = 1 M_{\odot}$ $\log(g) = +0.0$	$1\,690^{+2810}_{-1120}$ pc - -

**Notes.** The boldface distances correspond to the most likely values found by our stellar parameter analysis.



**Fig. 5.** Zoom into the H-R diagram where C-stars are located. The solar metallicity isochrones (Marigo et al. 2008) are plotted in grey and the small numbers indicate the predicted present mass. The sampling of points in the isochrones is shown with tiny squares. The position of the C-stars is indicated by a shaded area, the uncertainty about this area is discussed in Sect. 5. The different symbols plotted correspond to the parameters determined for every star and distance assumed: plus for CR Gem, asterisk for HK Lyr, diamond for RV Mon, triangle for Z Psc, and square for DR Ser.

the stellar evolution calculations (P. Marigo, priv. comm.), all stars on the cool side of the “hook” of the isochrones are C-stars. Some values of the present mass are marked on the isochrones: they will be compared with the mass of the best-fitting hydrostatic models (see Sect. 7).

We overplot on the isochrones the points corresponding to the parameters we determined. Every star is indicated with a different symbol centred on the temperature and luminosity associated to the model: a plus for CR Gem, an asterisk for HK Lyr, diamond for RV Mon, triangle for Z Psc, and square for DR Ser. The error bars of the temperature are the ones associated to the short  $L$  band  $T_{\text{eff}}$  determination, therefore, they are centred on

the  $T_{\text{eff}}$  (short  $L$ ) values given in Col. 3 of Table 3. The errors on the luminosity are not plotted here to avoid confusion but they are of the order of 40% (corresponding to the uncertainty on the distance measurements  $d_{\text{Berg}}$ ,  $d_{\text{Clau}}$ ).

## 6. Discussion of individual targets

### 6.1. CR Gem

CR Gem is classified as an irregular Lb variable with a variability amplitude in the  $B$ -band of 1.20 mag in the General Catalogue of Variable stars (GCVS; Samus+ 2007–2009). Nevertheless, Whitelock et al. (2008) classify this star as SRb with a period of 250<sup>d</sup> and the ASAS  $V$  band light curve shows an amplitude of 0.5 mag (Pojmanski 2002). The spectral classification given in the GCVS is C8,3e(N).

The  $3\ \mu\text{m}$  short  $L$  temperature we determine is around 100 K higher than the 2960 K measured by Bergeat & Chevallier (2005). The C/O we get is 1.05, we could not find other estimates for this value in the literature. The observed spectrum is presented in Fig. 6. It is in general well reproduced with a few exceptions: the range 1.2–1.4  $\mu\text{m}$  and the  $K$ -band between 2.1 and 2.3  $\mu\text{m}$ , where the real data show an excess compared to the models (see general discussion in Sect. 7).

For this star we collected only one point of PTI visibility (Fig. 6 lower right panel), therefore it is not possible to check for asymmetries. All visibility profiles corresponding to the Hipparcos distance are not extended enough to fit the visibility point, therefore this distance can be excluded. For the Claussen distance the best-fitting model has mass  $1 M_{\odot}$  and  $\log(g) = -0.60$ , the luminosity is  $9000 L_{\odot}$  and the radius of the star  $330 R_{\odot}$ . For the Bergeat distance, the highest value of distance estimated for this star, the best-fitting model has  $2 M_{\odot}$  and  $\log(g) = -0.4$ , the luminosity is  $11\,000 L_{\odot}$ , and the radius  $370 R_{\odot}$ .

### 6.2. HK Lyr

According to the GCVS, the visual amplitude of HK Lyr is 1.80 mag, the spectral classification C6,4(N4), and the star is classified as irregular Lb. The Hipparcos Variability Annex

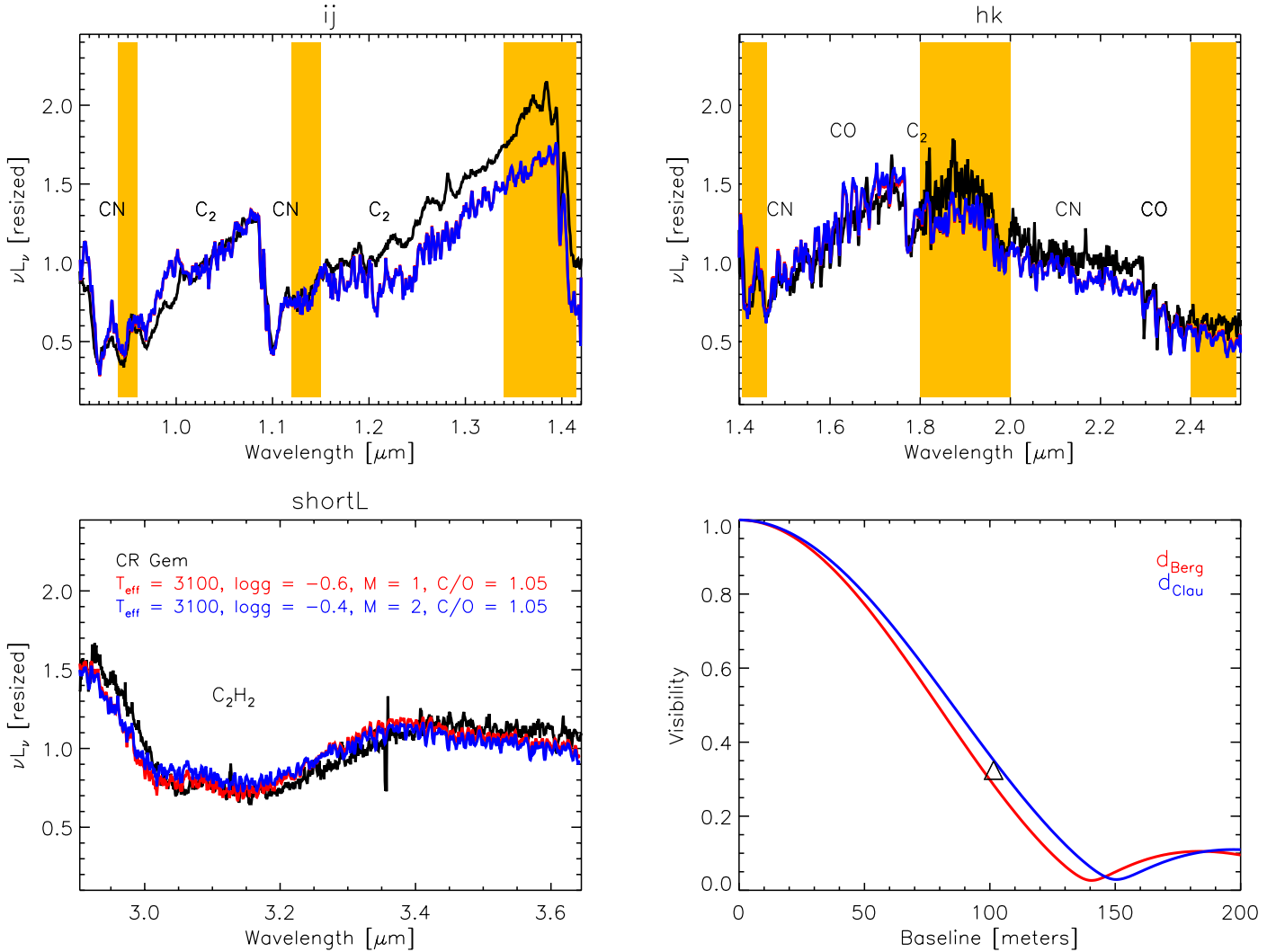


**Fig. 6.** Comparison of the UKIRT/UIST spectra (black line) and PTI interferometric measurements (black triangle) of CR Gem with hydrostatic model predictions. The *upper left panel* illustrates the *IJ* range of the spectrum, the *upper right panel* shows the *HK* wavelength range. The *lower left panel* shows the short *L* range. The shaded bands mark the region with poor atmospheric transmission. The molecules that contribute to the spectrum are also indicated. The synthetic spectra are overplotted in grey (blue, and red in the electronic version). The *lower right panel* shows the interferometric data point with the models which best fit the data for different distances overplotted.

(Beichman et al. 1988) reports for this star a period of 196<sup>d</sup> and an amplitude of variability of 0.4 in the Hipparcos magnitude. From optical spectroscopic analysis, this star is enriched in lithium and technetium (Abia et al. 2002; Boffin et al. 1993).

From our spectroscopic investigation the temperature and C/O ratio, obtained are higher than the ones estimated in literature (Table 3). While our temperature is 3080 K, Ohnaka & Tsuji (1996) give 2866 K and Bergeat & Chevallier (2005) estimate 2945 K. Concerning the C/O ratio we obtain 1.4, while Abia et al. (2002) estimate 1.02. The fit of the spectroscopic data is quite successful except for the region between 1.2 and 1.45  $\mu\text{m}$  (Fig. 7 upper left panel).

Eight visibility points are available from PTI observations. The UD diameters computed by fitting the single points do not differ. Over the time interval and position angle of the observations, the star does show no notable variation nor evidence of asymmetries (Fig. 2, row “b”). We fitted all visibility points with synthetic profiles scaled for different distances (Fig. 7 lower right panel).

None of the models corresponding to the Hipparcos distance can fit the points, therefore we excluded this distance.

The best-fitting parameters corresponding to  $d_{\text{Berg}}$  are  $2 M_{\odot}$  and  $\log(g) = -0.2$ . This model has a luminosity of  $L = 7200 L_{\odot}$  and a radius  $R = 300 R_{\odot}$ . The best-fitting model corresponding to  $d_{\text{Claui}}$  has again mass  $2 M_{\odot}$  but  $\log(g) = -0.4$ . This model has a luminosity of  $L = 11\,400 L_{\odot}$  and a radius  $R = 370 R_{\odot}$ . In Fig. 5 the resulting parameters for HK Lyr are plotted with asterisks.

### 6.3. RV Mon

RV Mon is a C4,4-C6,2(NB/R9) star, its variability class is SRb with a primary pulsation period of 131<sup>d</sup> and a long secondary period detected by Houk (1963) of 1047<sup>d</sup>. The amplitude of variability given in the GCVS is 2.19 mag in the *B*-band, while the ASAS light curve suggests a *V* amplitude of 0.3 mag.

The temperature obtained with our fitting procedure is between the values given in the literature. Ohnaka & Tsuji (1996) get  $T_{\text{eff}} = 3330$  K, we obtained 3170 K while Bergeat & Chevallier (2005) give 2910 K. No estimation of C/O was found in the literature to be compared with our 1.05. The model we adopted for RV Mon matches the spectroscopic observations in all ranges quite well except for the region of the CO bands

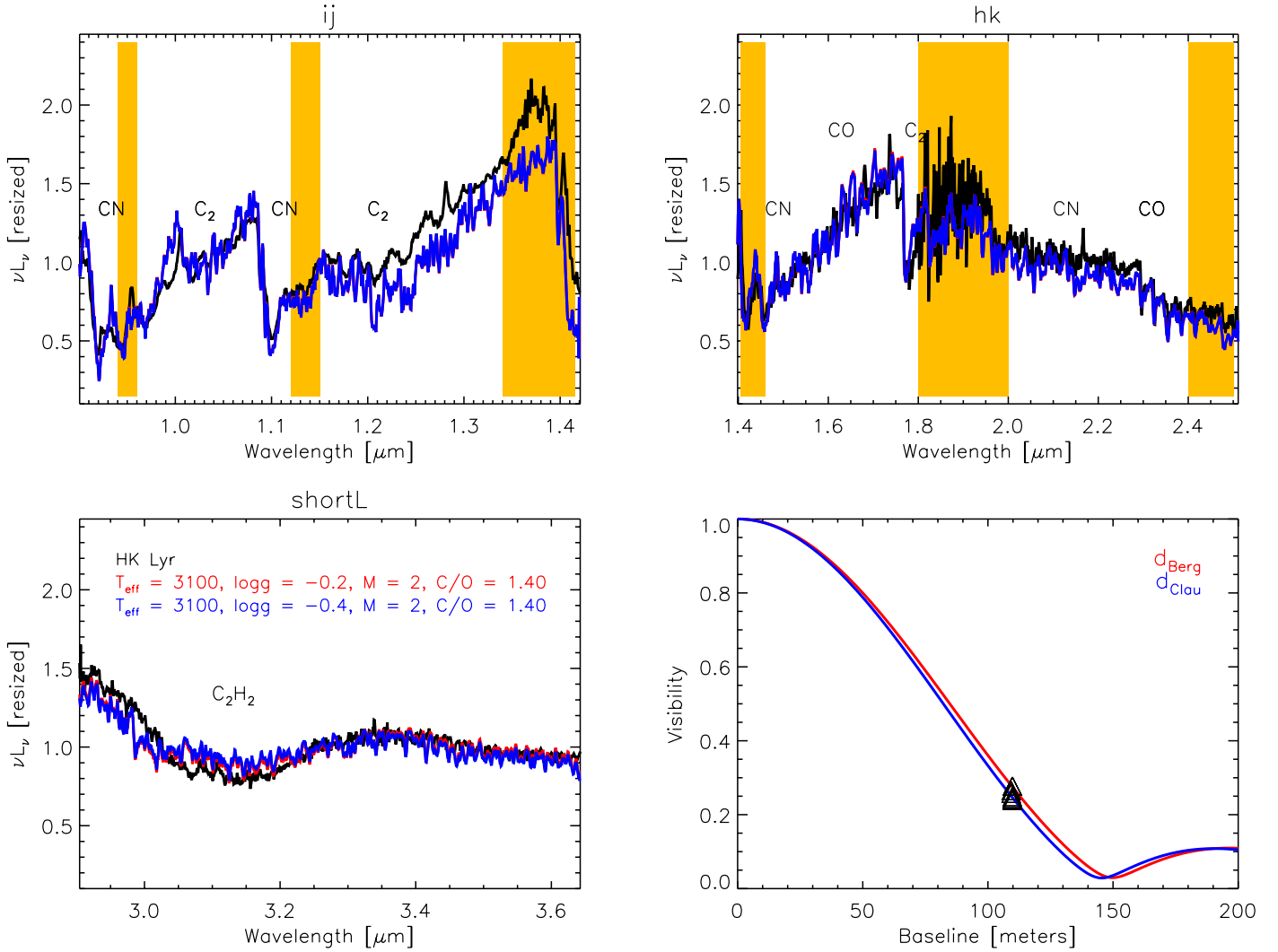
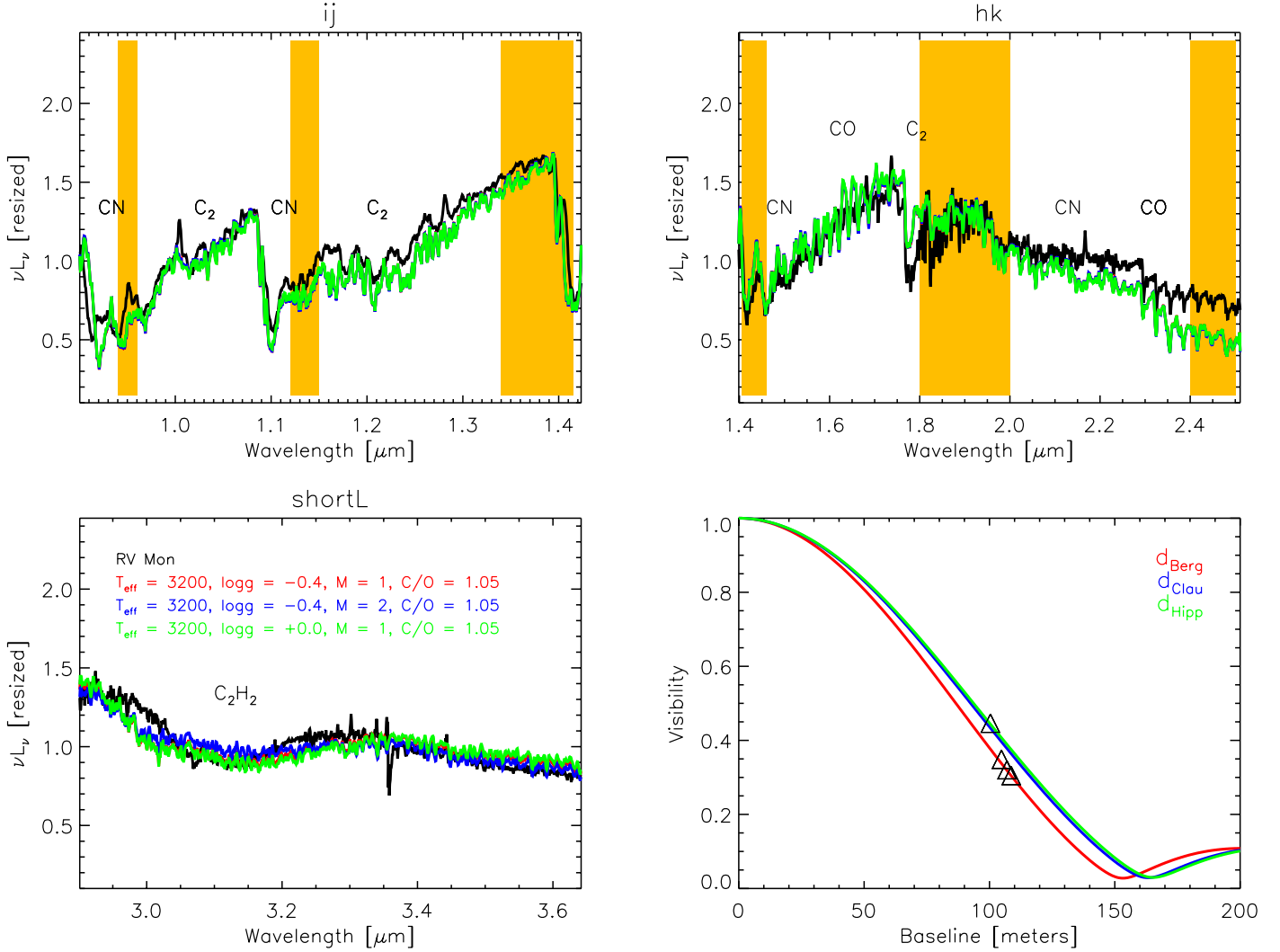


Fig. 7. Same as in Fig. 6 for HK Lyr.

(longward  $2.29 \mu\text{m}$ ), where the observations show an IR excess compared to the synthetic spectra. The intensity of the  $\text{C}_2$  feature at  $1.77 \mu\text{m}$  is not well reproduced but this is at the border of an atmospheric window.

For this star we collected four visibility points. The first one is in 1999, the other three in 2008. Although the observations were carried out at very similar baseline, the visibility jumps by 0.1 between the two epochs of observation. This jump is visible also in the UD-diameter where it amounts to  $\sim 0.16 \text{ mas}$ , which is larger than the estimated error on the UD diameters ( $\sim 0.06$  in the worst case). This difference is also noted in the plot of the UD-versus-position angle. A careful check was performed to exclude any problem coming from the calibration procedure, but still we cannot completely exclude that the fluctuation in the visibility is caused by an instrument problem. From the astrophysical point of view, the observed trend could be explained in different ways: (i) it could be an asymmetry plus a temporal variation (for example a large convective shell), (ii) or an effect of the pulsation (panel “4c”). The temporal variation caused by the primary short period of variability is not enough to explain the jump in the visibility. We derived from the light curve a difference in phase for the primary period of 0.16 between the two sets of observations. According to the predictions of the dynamic

model atmospheres (Paladini et al. 2009, see Figs. 7 and 9), a hot C-star should show a difference in UD-diam of  $0.06 \text{ mas}$ , definitely smaller than  $0.16$ . The two sets of observations have been obtained with a time difference of 3.5 times the length of the long secondary period. This longterm variation may, therefore, be responsible for the observed variation in size. Additional observations are necessary to reach a conclusive interpretation. Keeping this in mind, we performed a fit of the interferometric points with a hydrostatic model atmosphere as a first step. This might be followed by more investigations. From the lower right panel of Fig. 8 it is immediately obvious that no synthetic visibility profile can fit all observations at the same time. The best-fitting model obtained for the Hipparcos or Claussen distances can only fit the single point observed in 1999. The other models are either too extended or not extended enough to fit the other observations. The best-fitting model for  $d_{\text{Hipp}}$  has  $M = 1 M_{\odot}$ ,  $\log(g) = +0.0$ ,  $L = 2600 L_{\odot}$  and  $R = 170 R_{\odot}$ . For the distance determined by Claussen et al. (1987) the single data point is fitted by the model with  $2 M_{\odot}$ ,  $\log(g) = +0.4$ ,  $L = 13\,000 L_{\odot}$  and a radius  $R = 370 R_{\odot}$ . On the other hand, for the distance determined by Bergeat & Chevallier (2005) the three points observed in 2008 are fitted by the model with  $M = 1 M_{\odot}$ ,  $\log(g) = -0.4$ ,  $L = 6400 L_{\odot}$ , and  $R = 260 R_{\odot}$ . Nevertheless, the effect of



**Fig. 8.** Same as in Fig. 6 for RV Mon.

variability or possible asymmetries needs to be investigated in more detail, and the parameters derived for this object should be considered with caution.

#### 6.4. Z Psc

Z Psc is an SRb variable with amplitude derived from photographic plates of 1.3 mag. The period in the GCVS is 144<sup>d</sup>. The ASAS light curve has an amplitude of 0.52 mag in V band. The spectral classification from the GCVS (Samus+ 2007–2009) is C7,2(N0). Abia et al. (2002), and Boffin et al. (1993) determined a <sup>12</sup>C/<sup>13</sup>C = 55, moreover, they found enhancement of Tc, and no trace of Li in the spectrum. This implies that Z Psc is a standard low-mass TP-AGB star, and an intrinsic C-rich star.

Many temperature estimates were given for this star in the literature: Lambert et al. (1986) obtained 2870 K, Dyck et al. (1996) 3240 K, Ohnaka & Tsuji (1996) 3150 K, Bergeat & Chevallier (2005) 3095 K. All these values were obtained with different methods. Our measurement (see Table 3) is very close to the one given by Ohnaka & Tsuji (1996). The C/O = 1.05 we estimated agrees with the 1.014 of Lambert et al. (1986) and with the more recent 1.01 value of Abia et al. (2010). The match between models and observations is shown in Fig. 9. From spectroscopy a small disagreement is barely detectable in the C<sub>2</sub> band

at 1.20 μm, while the 3 μm feature of the model is too deep to fit the data (the star is hotter than the model).

Z Psc is the only one among our targets with no PTI data. For this star we used an observation available from the literature (Dyck et al. 1996) taken in the K-broad band with IOTA (2.2 μm) as already described in Sect. 2.2. The fit of the interferometric IOTA data is presented in the lower right panel of Fig. 9. The best-fitting model for the Hipparcos distance has a mass  $M = 1 M_{\odot}$ ,  $\log(g) = +0.0$ ,  $L = 2300 L_{\odot}$ , and  $R = 165 R_{\odot}$ . The distance determined by Bergeat & Chevallier (2005) gives a best-fitting model with the same  $\log(g)$  obtained for Hipparcos distance fit but  $M = 2 M_{\odot}$ ,  $L = 4500 L_{\odot}$  and a radius  $R = 230 R_{\odot}$ . In the case of the Claussen distance we have the best-fitting, which is the model with mass  $1 M_{\odot}$ ,  $\log(g) = -0.5$ ,  $L = 7150 L_{\odot}$ , and  $R = 300 R_{\odot}$ .

#### 6.5. DR Ser

According to the GCVS, DR Ser is an irregular variable Lb with an amplitude in the B-band of 2.99 mag. The ASAS light curve of this object is quite stable over the last 2000 days, it has a period of 196<sup>d</sup>, and a V band amplitude of 0.3 mag. The spectral class is C6,4(N).

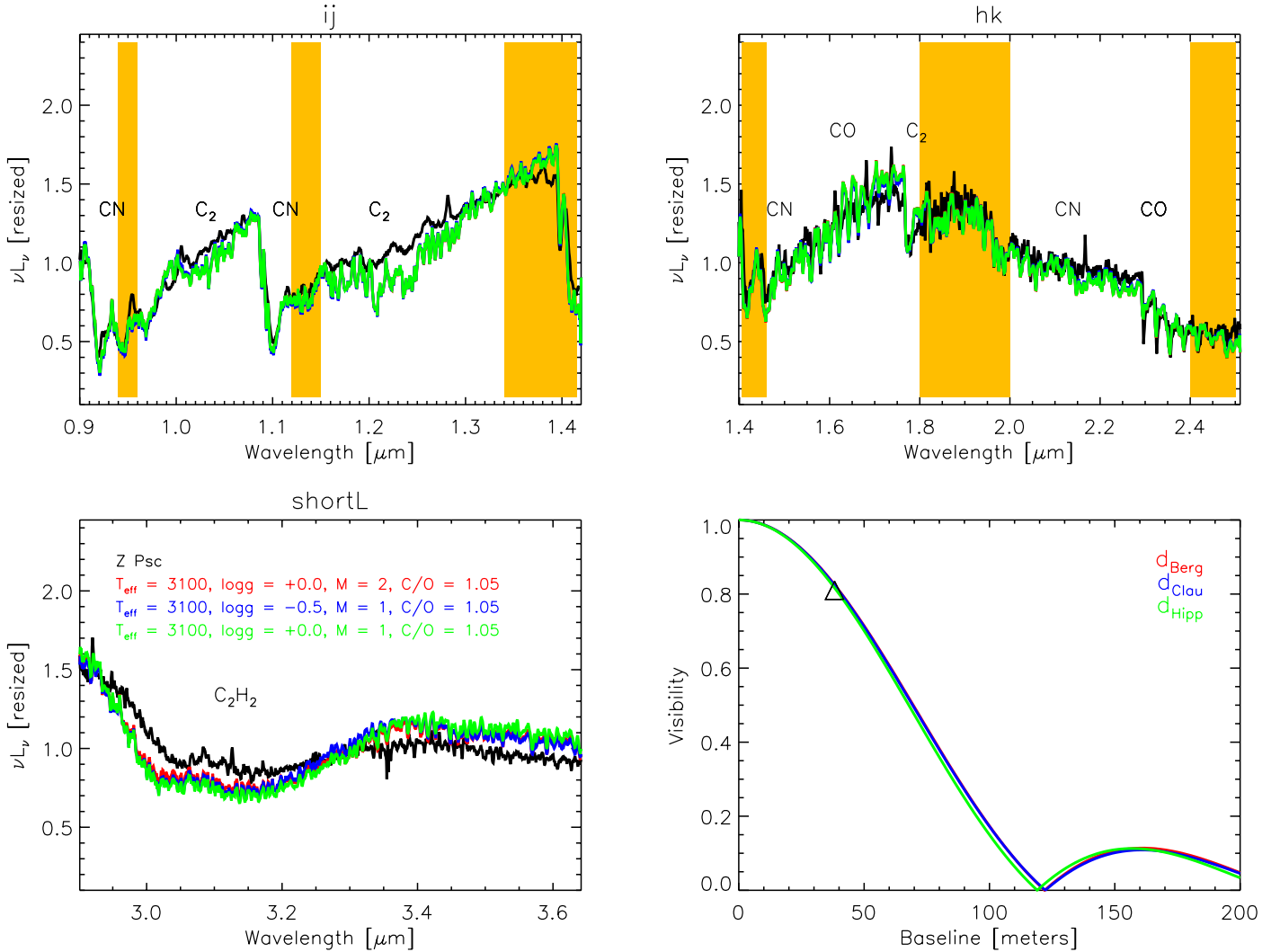


Fig. 9. Same as in Fig. 6 for Z Psc.

This object is the one in our sample with the highest value of interstellar reddening. Applying the reddening correction, we noted that the observed spectrum looks completely unrealistic. Remembering that reddening correction for single objects is always very uncertain, we decided to skip the step of the reddening correction for DR Ser. Further investigation and a detailed map of the ISM in the region of this star are needed.

We determined a temperature of 3080 K. In the literature the  $T_{\text{eff}}$  values associated to this object are usually lower (see Sect. 7): 2500 K (Abia & Isern 1997), 2570 K (Thompson et al. 2002), 2650 K (Schöier et al. 2005; Bergeat & Chevallier 2005). Abia & Isern (1997) estimated the isotopic ratio  $^{12}\text{C}/^{13}\text{C} = 6$ , which is also surprisingly low! The C/O we found, 1.05 is lower than the C/O = 1.26 obtained in literature by Eglitis & Eglite (1995).

There are 54 PTI points available for this object in the period between June 2000 and August 2001. The UD diameters determined agree with each other within a range of  $\pm 0.02$  mas, therefore we considered for the model fitting all points together (Fig. 10). None of the profiles computed at the Hipparcos distance could fit the data points. The best-fitting models have a mass  $M = 2 M_{\odot}$ , and  $\log(g) = -0.4$  or  $-0.6$  for  $d_{\text{Clau}}$  and  $d_{\text{Berg}}$  respectively. The first model has  $L = 11\,400 L_{\odot}$  and a radius of  $370 R_{\odot}$ ; the second one  $L = 18\,000 L_{\odot}$  and  $R = 470 R_{\odot}$ . It is

impressive to note how all the visibility points observed at different epochs and position angles fit the hydrostatic synthetic profile.

## 7. Discussion

Based on the fitting procedure described above, we can identify a sequence in effective temperature for our targets. The temperature increases, starting from CR Gem, DR Ser, HK Lyr, Z Psc, RV Mon. Our temperature determination is very precise thanks to the large grid of models available and to the use of the short  $L$  band spectrum. The  $T_{\text{eff}}$  here determined are always compatible within the error given in the literature.

The C/O ratio determination is not as accurate as the one of the temperature because of the very coarse spacing in the model grid, but mainly because of the low resolution of the spectra. Although the C/O values we determine have to be considered as indicative, they agree quite well with the ones estimated in the literature. We obtained the same C/O = 1.05 for all the stars except HK Lyr, which has C/O = 1.4. Those values agree with the range [1.01, 1.4] reported in the literature for classical C-stars (see Fig. 42 of Lambert et al. 1986; and Table 2 of Bergeat & Chevallier 2005).

In general there is a good agreement between synthetic and observed spectra. Small discrepancies are observed mainly in the

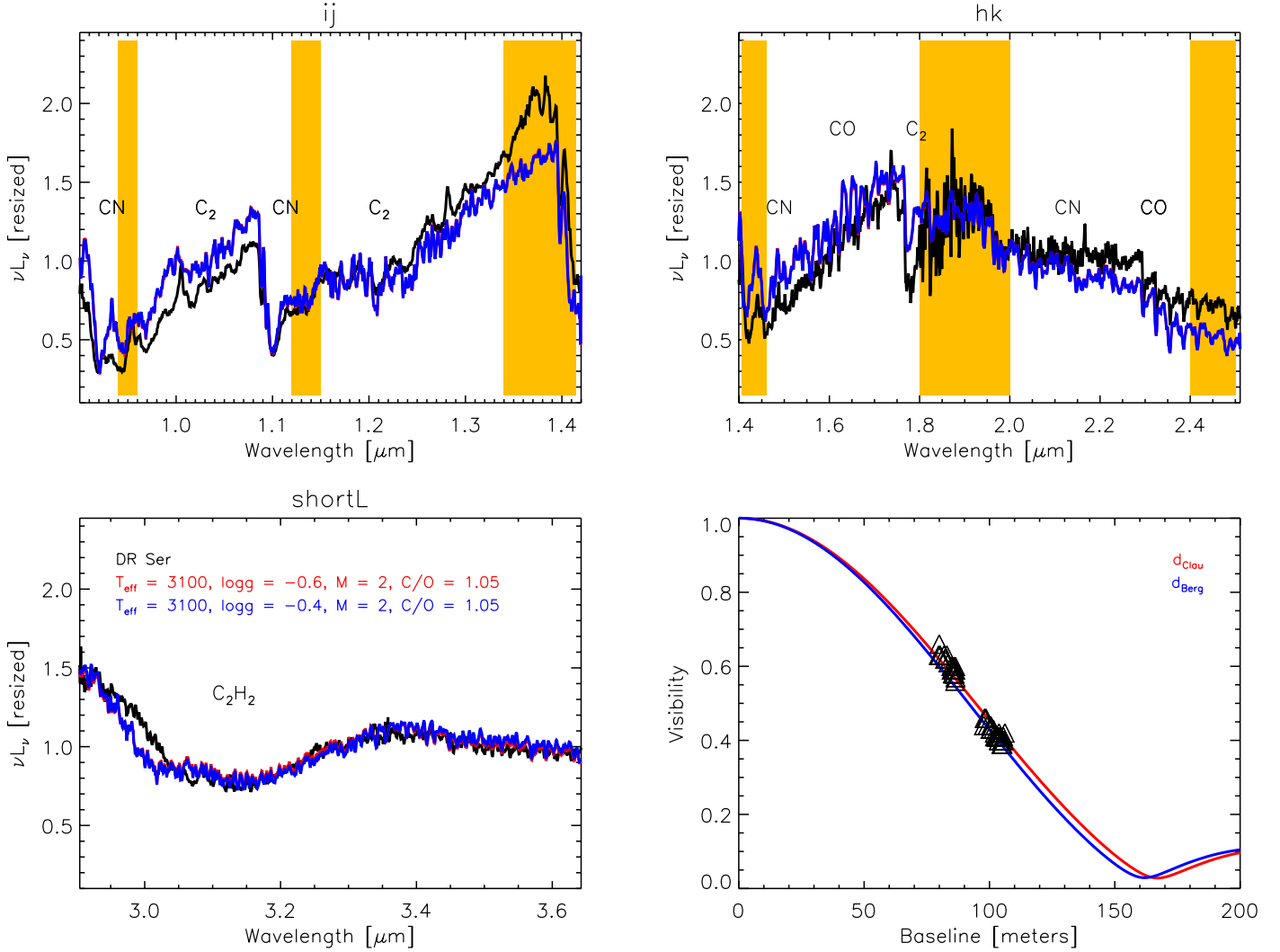


**Fig. 10.** Same as in Fig. 6 for DR Ser.

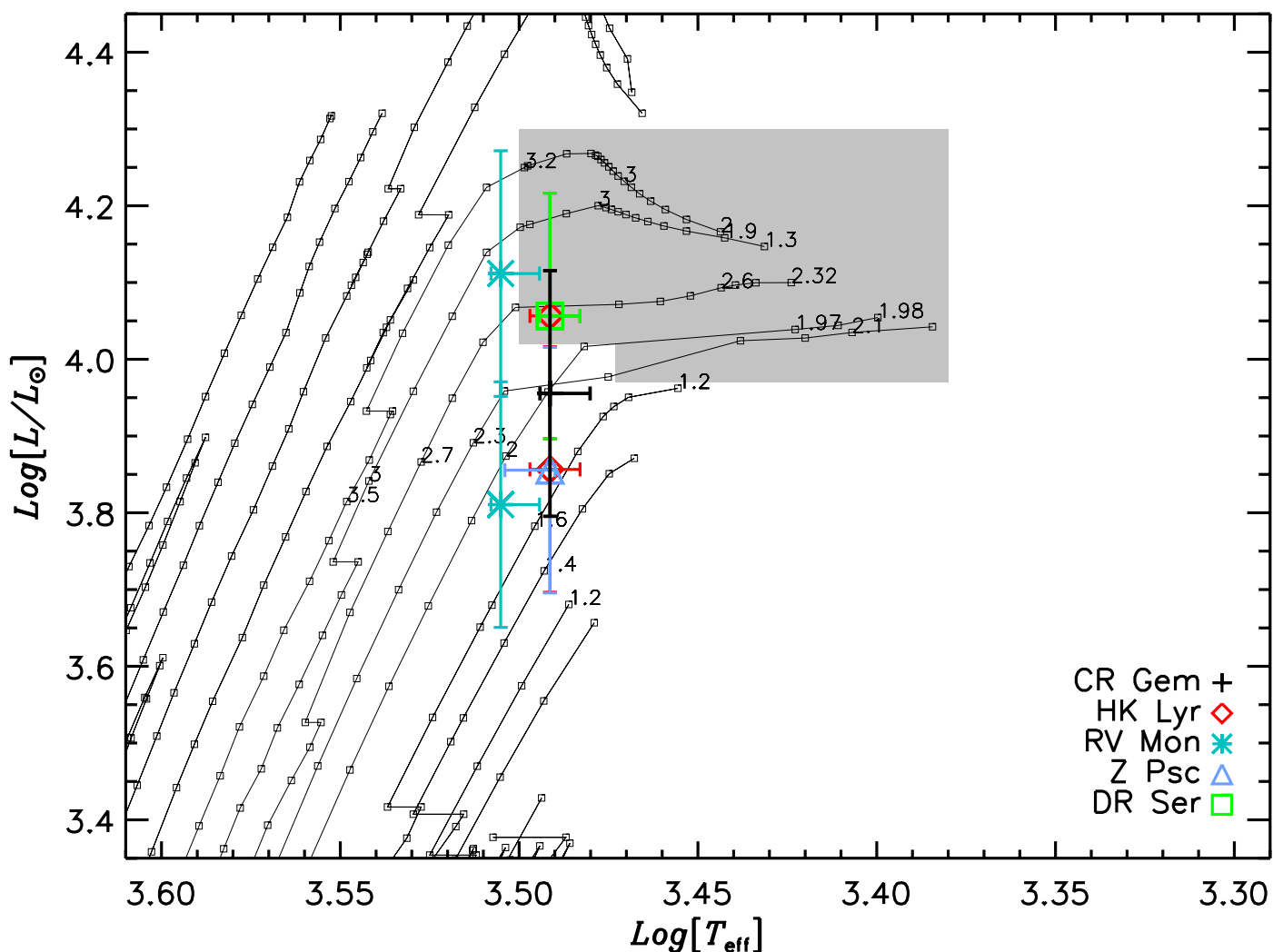
region between 1.2 and 1.4  $\mu\text{m}$ , between 2.1 and 2.3  $\mu\text{m}$  and on the left edge of the 3  $\mu\text{m}$  feature. They can be attributed to small calibration problems, but also to a small amount of dust. This last point is supported by the fact that the differences detected in the *IJ* band between 1.2 and 1.4  $\mu\text{m}$  are larger for the lower temperature stars (CR Gem, HK Lyr, DR Ser). We simulated the effect on the spectrum of a small amount of dust by using the DUSTY code (Ivezic & Eliztur 1997). Indeed, the *IJ* band of the spectrum fits slightly better for stars that have a high *J* – *K* value (CR Gem, DR Ser). We also checked the effect of this small amount of dust on the stellar parameter determination. The effect on the temperature and on the interferometric observable was within the error bar we already took into account, therefore we proceed with the hydrostatic models. A detailed analysis of spectro-interferometric observations with a hydrostatic+dusty model atmosphere will be presented in a follow-up work.

From the fit of the interferometric observations with models at different distances we note that in three of five cases no model can fit the observations at the distance estimated from Hipparcos. This is not such a surprise considering the error associated to these distance measurements. Further consideration about the distance can be made by studying the position of the best-fitting models in the H-R diagram (Fig. 5).

Some of our hydrostatic models lie in a region of the H-R where larger masses are expected. If we consider the agreement

between the two masses (from hydrostatic models and evolutionary calculations) as a criterion to select the correct distance of the objects, we have

- CR Gem. The point with lower luminosity is the one fitting the range of mass, therefore the distance determined by Claussen can be retained, and the one of Bergeat discarded.
- HK Lyr. Both models have the same mass and lie in a region in between 1 and 2.6  $M_{\odot}$ . Considering an error on both distances of 20% (i.e. a factor 1.44 in luminosity), none of the values can be excluded.
- RV Mon. The Hipparcos distance is in the correct region of mass, but too far from the C-stars region, therefore it can be discarded. Both the other two distances correspond to a model that fits the region of masses, therefore they can be both retained.
- Z Psc. In this case the Bergeat distance can be discarded because the best-fitting model has 2  $M_{\odot}$ , but falls in the range of 1  $M_{\odot}$ . Considering the error on the luminosity, both the distances from Hipparcos and Claussen can be retained. Nevertheless, the position of the model at the Claussen distance is more probable because this is closer to the C-stars region.
- DR Ser. The distance estimated from Bergeat can be discarded because the model lies in the region of the stars with 3  $M_{\odot}$ .

$Z = 0.019$ 

**Fig. 11.** Same as in Fig. 5, but this time only the parameters with most probable distances are plotted.

The parameters with the most probable distances, with associated errors in temperature and luminosity are shown in Fig. 11.

Taking into account the uncertainty associated to the transition phase M-C stars (see Sect. 5), all stars have at least one combination of parameters that lie in the region where the C-stars sequence starts. This agrees with the hydrostatic scenario for our targets: the objects are supposed to be hot C-stars, with relatively low mass-loss and low C/O. They “recently” turned into C-stars, and while moving on the evolutionary track, they will increase the production of carbon and will lose more and more mass because of the stellar wind. Our work is partially limited because that only model atmospheres with mass 1 and 2 are available.

Two objects of our sample show some peculiarity that deserves additional investigations. The interferometric observations of RV Mon show a possible non-hydrostatic nature. All visibility points acquired with PTI cannot be fitted with the same model. This might be caused by some instrumental effect, while the physical explanation would be an evidence of an asymmetry or (more probably) of a variability effect. According to the interferometric measurements, the star DR Ser is a hydrostatic object. We were able to fit with the same model 54 visibility points observed in different epochs and position angles. On the other hand, the fit of the *IJ* and *HK* band is not very good, and the

reddening correction of the spectrum makes the fit even worse. A detailed ISM map for this region of the sky is needed.

## 8. Conclusions

More than a simple parameters determination, this work aims to identify which of the stellar parameters of C-stars can be constrained by using different techniques like spectroscopy and interferometry. Which limits appear by investigating only with one tool? Infrared interferometry is a relatively young field of research, but it can already give a significant contribution to the stellar parameter determinations.

We confirm that low-resolution infrared spectroscopy is not sensitive to  $\log(g)$  and mass determinations of C-stars. We clearly show that a highly precise determination of the temperature can be achieved for C-stars with no significant dust contribution thanks to the use of the  $3\ \mu\text{m}$  feature ( $\text{C}_2\text{H}_2 + \text{HCN}$ ). The determinations based only on the *IJH* bands tend to underestimate the temperature.

The hydrostatic model atmospheres adopted in this work were able for the first time to fit simultaneously spectroscopic and interferometric observations. This is a very important achievement considering that inaccuracies in model atmospheres reflect negatively on the check of the stellar evolution

calculations. On the other hand, the inaccuracy in the distance determination for this class of objects reflects negatively on the parameter determination, as already noted in Wittkowski et al. (2001). We considered a criterion to select the distance on the agreement between mass of the hydrostatic models and mass predicted by the isochrones. According to this, the distance estimated by Clausen et al. (1987) is the most probable among the three distances we used for this work. Taking into account the uncertainty in the transition phase from O-rich to C-rich star in the evolution models as well, we obtained that all the objects of our sample have at least one combination of observationally determined parameters that fits the C-stars region. We were able to associate temperature, C/O, mass,  $\log(g)$  and a range of reasonable distances for all objects of our sample.

A grid of models with larger coverage of the mass range (at least from 1 to 4  $M_{\odot}$ ) as well as a more dense grid of points for the isochrones would significantly improve our estimations. The advent of a new dedicated mission (Gaia) might improve the distance problem for C-stars.

The synergy between different techniques of investigation and realistic theoretical atmospheric and stellar evolutionary models will be the key to determine precise characteristics for this class of objects, and to be able to understand clearly the physical processes that drive their evolution.

*Acknowledgements.* The authors acknowledge the anonymous referee for useful comments that helped improve the paper. This work is supported by the Projects P19503-N16 of the Austrian Science Fund (FWF). B.A. acknowledges funding by the contract ASI-INAF I/016/07/0, and ASI-INAF I/009/10/0. T.L. acknowledges support through the FWF-project P20046-N16. The United Kingdom Infrared Telescope is operated by the Joint Astronomy Centre on behalf of the Science and Technology Facilities Council of the UK Science operations with PTI were conducted through the efforts of the PTI Collaboration (<http://pti.jpl.nasa.gov/ptimembers.html>) and the National Aeronautics and Space Administration (NASA) Exoplanet Science Institute (NExScI), and we acknowledge the invaluable contributions of our PTI colleagues. We particularly thank Kevin Rykoski for his professional operation of PTI. PTI was constructed with funds from the Jet Propulsion Laboratory, Caltech, as provided by NASA. We acknowledge D. V. Shulyak for computing the models for the standard stars, P. Marigo and W. Nowotny for the useful discussions, A. Baier and S. Sacuto for helping with Dusty Code, L. Pavan for useful discussions on the reddening correction. The research leading to these results has received funding from the European Community's Seventh Framework Programme under Grant Agreement 226604.

## References

- Abia, C., & Isern, J. 1997, MNRAS, 289, 11  
 Abia, C., Domínguez, I., Gallino, R., et al. 2002, ApJ, 579, 817  
 Abia, C., Cunha, K., Cristallo, S., et al. 2010, ApJ, 715, 94  
 Amôres, E. B., & Lépine, J. R. D. 2005, AJ, 130, 659  
 Aringer, B. 2000, Ph.D. Thesis, University of Vienna  
 Aringer, B., Jørgensen, U. G., & Langhoff, S. R. 1997, A&A, 323, 202  
 Aringer, B., Girardi, L., Nowotny, W., Marigo, P., & Lederer, M. T. 2009, A&A, 503, 913  
 Aufdenberg, J., Ridgway, S., & White, R. 2009, in *astro2010: The Astronomy and Astrophysics Decadal Survey*, Science White Papers, astro2010S, 8  
 Bagnulo, S. 1996, Ph.D. Thesis, Belfast University  
 Beichman, C. A., Neugebauer, G., Habing, H. J., Clegg, P. E., & Chester, T. J. 1988, NASAR, 1190, 1  
 Bergeat, J., & Chevallier, L. 2005, A&A, 429, 235  
 Bergeat, J., Knapik, A., & Rutily, B. 2002, A&A, 390, 967  
 Boden, A. F., Colavita, M. M., van Belle, G. T., & Shao, M. 1998, Proc. SPIE, 3350, 872  
 Boden, A. F., Koresko, C. D., van Belle, G. T., et al. 1999, ApJ, 515, 356  
 Boffin, H. M. J., Abia, C., & Rebolo, R. 1993, A&AS, 102, 361  
 Cavanagh, B., Hirst, P., Jenness, T., et al. 2003, ASPC, 295, 237  
 Clausen, M. J., Kleinmann, S. G., Joyce, R. R., & Jura, M. 1987, ApJS, 65, 385  
 Colavita, M. M., Wallace, J. K., Hines, B. E., et al. 1999, ApJ, 510, 505  
 Cutri, R. M., Skrutskie, M. F., van Dyk, S., et al. 2003, in *The IRSA 2MASS All-Sky Point Source Catalog*, NASA/IPAC Infrared Science Archive  
 Dyck, H. M., van Belle, G. T., & Benson, J. A. 1996, AJ, 112, 294  
 Eglitis, I., & Eglite, M. 1995, Ap&SS, 229, 63  
 Epchtein, N., Le Bertre, T., & Lepine, J. R. D. 1990, A&A, 227, 82  
 Erspamer, D., & North, P. 2003, A&A, 398, 1121  
 García-Hernández, D. A., García-Lario, P., Plez, B., et al. 2007, A&A, 462, 711  
 Gautschy-Loidl, R., Höfner, S., Jørgensen, U. G., & Hron, J. 2004, A&A, 422, 289  
 Goorvitch, D., & Chackerian, Jr. C. 1994, ApJS, 91, 483  
 Gustafsson, B., Bell, R. A., Eriksson, K., & Nordlund1975, A&A, 42, 407  
 Gustafsson, B., Edvardsson, B., Eriksson, K., et al. 2008, A&A, 486, 951  
 Harris, G. J., Tennyson, J., Kaminsky, B. M., Pavlenko, Y. V., & Jones, H. R. A. 2006, MNRAS, 367, 400  
 Hauschildt, P. H., Allard, F., Ferguson, J., Baron, E., & Alexander, D. R. 1999, ApJ, 525, 871  
 Houk, N. 1963, AJ, 68, 253  
 Iben, I., & Renzini, A. 1983, ARA&A, 21, 271  
 Ivezić, Z., & Elitzur, M. 1997, MNRAS, 287, 799  
 Jørgensen, U. G. 1997, in *Molecules in Astrophysics: Probes and Processes*, ed. E. F. van Dishoeck (Kluwer), IAU Symp., 178, 441  
 Jørgensen, U. G., Almlöf, J., & Siegbahn, P. E. M. 1989, ApJ, 343, 554  
 Jørgensen, U. G., Johnson, H. R., & Nordlund 1992, A&A, 261, 263  
 Jørgensen, U. G., Hron, J., & Loidl, R. 2000, A&A, 356, 253  
 Kerschbaum, F., Lazaro, C., & Habison, P. 1996a, A&AS, 118, 397  
 Kerschbaum, F., Olofsson, H., & Hron, J. 1996b, A&A, 311, 273  
 Kervella, P., Thévenin, F., Ségransan, D., et al. 2003, A&A, 404, 1087  
 Kurucz, R. L. 1993, ASPC, 44, 87  
 Lambert, D. L., Gustafsson, B., Eriksson, K., & Hinkle, K. H. 1986, ApJS, 62, 373  
 Lederer, M. T., & Aringer, B. 2009, A&A, 494, 403  
 Lester, J., & Neilson, H. 2008, A&A, 491, 633  
 Loidl, R., Lancon, A., & Jørgensen, U. G. 2001, A&A, 371, 1065  
 Marigo, P., Girardi, L., Bressan, A., et al. 2008, A&A, 482, 883  
 Masana, E., Jordi, C., & Ribas, I. 2006, A&A, 450, 735  
 Mattsson, L., Wahlin, R., & Höfner, S. 2010, A&A, 509, 14  
 Mozurkewich, D., Johnston, K. J., Simon, R. S., et al. 1991, AJ, 101, 2207  
 Neilson, H. R., & Lester, J. B. 2008, A&A, 490, 807  
 Nowotny, W., Lebzelter, T., Hron, J., & Höfner, S. 2005, A&A, 437, 285  
 Nowotny, W., Höfner, S., & Aringer, B. 2010, A&A, 514, 35  
 Nowotny, W., Aringer, B., Höfner, S., & Lederer, M. T. 2011, A&A, 529, 129  
 Ohnaka, K., & Tsuji, T. 1996, A&A, 310, 933  
 Paladini, C., Aringer, B., Hron, J., et al. 2009, A&A, 501, 1073  
 Peryman, M. A. C., Lindegren, L., Kovalevsky, J., et al. 1997, A&A, 323, 49  
 Pojmanski, G. 2002, Acta Astron., 52, 397  
 Querci, F., Querci, M., & Tsuji, T. 1974, A&A, 31, 265  
 Ramsay Howat, S., Todd, S., Legget, S., et al. 2004, Proc. SPIE, 5492, 1160  
 Samus, N. N., Durevich, O. V., et al. 2009, General Catalogue of Variable Stars, yCat, 102025S  
 Schöier, F. L., Lindqvist, M., & Olofsson, H. 2005, A&A, 436, 633, 646  
 Shulyak, D. V., Tsybmal, V., Ryabchikova, T., Stütz, Ch., & Weiss, W. W. 2004, A&A, 428, 993  
 Sloan, G. C., Little-Marenin, I. R., & Price, S. D. 1998, AJ, 115, 809  
 Solano, E., & Fernley, J. 1997, A&AS, 122, 131  
 Tanaka, M., Letip, A., Nishimaki, Y., et al. 2007, PASJ, 59, 939  
 Thompson, R. R., Creech-Eakman, M. J., & van Belle, G. T. 2002, ApJ, 577, 447  
 Tsuji, T. 1986, ARA&A, 24, 89  
 Utenthaler, S., & Lebzelter, T. 2010, A&A, 510, 62  
 van Belle, G. T., & van Belle, G. 2005, PASP, 117, 1263  
 van Belle, G. T., van Belle, G., Creech-Eakman, M. J., et al. 2008, ApJS, 176, 276  
 Vanture, A. D., Smith, V. V., Lutz, J., et al. 2007, PASP, 119, 147  
 Verhoolst, T. 2005, Ph.D. Thesis, University of Leuven  
 Wittkowski, M. 2004, Proc. of the 37th Liege International Astrophysical Colloquium, Science Case for Next Generation Optical/Infrared Interferometric Facilities (the post VLTI era)  
 Wittkowski, M., Hummel, C. A., Johnston, K. J., et al. 2001, A&A, 377, 981  
 Wittkowski, M., Aufdenberg, J. P., & Kervella, P. 2004, A&A, 413, 711  
 Wittkowski, M., Aufdenberg, J. P., Driebe, T., et al. 2006a, A&A, 460, 855  
 Wittkowski, M., Hummel, C. A., Aufderberg, J. P., & Roccatagliata, V. 2006b, A&A, 460, 843  
 Whitelock, P. A., Feast, M. W., & van Leeuwen, F. 2008, MNRAS, 386, 313

## Appendix A: Statistical approach at temperature determination

In order to assign an observed spectrum to one out of a sample of available models, a statistical approach is employed: each model represents a Gaussian-shaped sandheap the width of which (in terms of standard deviation) is determined by the point-to-point scatter  $p$  of the spectrum. The height of the sandheaps can be adjusted by statistical weights. Thus, the shape of the  $n$ th sandheap is given by the Gaussian probability density function

$$G(d_n) = \exp\left(-\frac{d_n^2}{2p^2}\right). \quad (\text{A.1})$$

The “distance”  $d_n$  between the observed spectrum and the model is the rms deviation between the observed and the synthetic spectrum. The statistical analogy of the model assignment is to pick out a single grain of sand at the given distances from the synthetic spectra. Now the question is, how high is the probability of the picked grain to belong to the  $n$ th sandheap?

The total number of available grains at the selected position is determined by the sum of densities for all  $N$  models,

$$\nu = \sum_{n=1}^N G(d_n), \quad (\text{A.2})$$

which represents our normalisation condition. Thus, the relative amount of grains belonging to model  $n$  – and hence

the probability of the observed spectrum to represent this model – evaluates to

$$\text{Pr}_n = \frac{G(d_n)}{\nu}. \quad (\text{A.3})$$

In the context of our application, the only parameter of interest is the effective temperature, whence the temperature interval covered by the models is divided into a set of intervals  $I_t$ ,  $t = 1, \dots, \tau$ . Because the number of models belonging to such a temperature bin is not unique, the marginal probability density of temperature has to be corrected for this bias. In the sandheap metaphor, we would have to provide each temperature interval to be represented by a unique number of grains, and the probability of our spectrum to be assigned to the temperature interval  $I_t$  evaluates to the weighted sum of individual model assignment probabilities

$$\text{Pr}(I_t) = \frac{m_t^{-1} \sum_{n=1}^{m_t} \text{Pr}_n(I_t)}{\sum_{i=1}^{\tau} m_i^{-1} \sum_{k=1}^{m_i} \text{Pr}_k(I_i)}, \quad (\text{A.4})$$

$m_t$  and denoting the number of models belonging to the interval  $I_t$ .

This normalisation is demonstrably valid, because the integral probability for all temperatures evaluates to

$$\sum_{t=1}^{\tau} \text{Pr}(I_t) = \frac{\sum_{t=1}^{\tau} m_t^{-1} \sum_{n=1}^{m_t} \text{Pr}_n(I_t)}{\sum_{i=1}^{\tau} m_i^{-1} \sum_{k=1}^{m_i} \text{Pr}_k(I_i)} = 1. \quad (\text{A.5})$$

**Table A.1.** Interferometric observations.

ID	UT Date	B [m]	PA [deg]	$V \pm \sigma_V$	Additional information
CR Gem	11/03/1999 Nov 3	101.49	80	$0.324 \pm 0.004$	
HK Lyr	1999 May 20	109.79	71	$0.277 \pm 0.004$	
	1999 May 21	109.78	78	$0.277 \pm 0.005$	
	2000 May 22	109.29	63	$0.258 \pm 0.005$	
	2000 May 22	109.33	64	$0.265 \pm 0.004$	
	2000 May 22	109.76	71	$0.238 \pm 0.010$	
	2000 May 22	109.77	72	$0.244 \pm 0.003$	
	2000 May 22	109.73	80	$0.249 \pm 0.003$	
	2000 May 22	109.72	81	$0.242 \pm 0.003$	
RV Mon	1999 Nov 04	100.37	63	$0.446 \pm 0.015$	
	2008 Sep 25	108.68	52	$0.305 \pm 0.005$	
	2008 Sep 25	106.98	55	$0.320 \pm 0.004$	
	2008 Sep 25	104.79	57	$0.349 \pm 0.006$	
Z Psc	1995 Oct 08	38.21	–	$0.810 \pm 0.123$	(1)
DR Ser	2000 Jun 03	106.29	55	$0.387 \pm 0.008$	
	2000 Jun 19	107.05	54	$0.535 \pm 0.024$	(2)
	2000 Jun 19	106.01	56	$0.497 \pm 0.035$	(2)
	2000 Jun 19	105.45	56	$0.487 \pm 0.032$	(2)
	2000 Jun 19	104.83	57	$0.515 \pm 0.024$	(2)
	2000 Jun 20	103.33	59	$0.435 \pm 0.013$	
	2000 Jun 20	102.19	60	$0.429 \pm 0.013$	
	2001 Apr 18	104.41	57	$0.407 \pm 0.010$	
	2001 Apr 18	104.20	58	$0.415 \pm 0.004$	
	2001 Apr 18	103.23	59	$0.407 \pm 0.003$	
	2001 Apr 18	103.06	59	$0.413 \pm 0.007$	
	2001 Apr 18	102.13	60	$0.410 \pm 0.005$	
	2001 Apr 23	106.14	55	$0.418 \pm 0.013$	
	2001 Apr 23	103.56	58	$0.410 \pm 0.012$	
	2001 Apr 23	100.63	62	$0.429 \pm 0.011$	
	2001 Apr 23	99.18	64	$0.435 \pm 0.011$	
	2001 Apr 23	97.73	66	$0.440 \pm 0.012$	
	2001 Apr 29	105.27	56	$0.389 \pm 0.006$	
	2001 Apr 29	105.01	57	$0.391 \pm 0.005$	
	2001 Apr 29	103.67	58	$0.396 \pm 0.005$	
	2001 Apr 29	102.84	59	$0.406 \pm 0.005$	
	2001 Apr 29	102.68	59	$0.407 \pm 0.008$	
	2001 May 03	86.43	15	$0.587 \pm 0.014$	
	2001 May 03	86.40	15	$0.597 \pm 0.015$	
	2001 May 03	85.92	15	$0.591 \pm 0.019$	
	2001 May 03	84.84	16	$0.593 \pm 0.018$	
	2001 May 03	83.03	17	$0.626 \pm 0.023$	
	2001 May 04	86.07	15	$0.583 \pm 0.009$	
	2001 May 04	85.98	15	$0.580 \pm 0.009$	
	2001 May 04	84.76	16	$0.599 \pm 0.010$	
	2001 May 04	82.50	17	$0.615 \pm 0.007$	
	2001 May 04	82.24	17	$0.621 \pm 0.011$	
2001 May 05	86.31	15	$0.589 \pm 0.006$		
2001 May 05	85.79	15	$0.598 \pm 0.007$		
2001 May 05	84.85	16	$0.605 \pm 0.005$		
2001 May 05	83.54	17	$0.613 \pm 0.008$		
2001 May 05	81.86	17	$0.626 \pm 0.006$		
2001 May 23	104.92	57	$0.402 \pm 0.007$		
2001 May 23	103.80	58	$0.416 \pm 0.004$		
2001 Jun 21	103.71	58	$0.404 \pm 0.006$		
2001 Jun 21	102.06	60	$0.420 \pm 0.005$		
2001 Jun 21	100.30	63	$0.433 \pm 0.005$		
2001 Jun 21	98.60	65	$0.460 \pm 0.009$		
2001 Jul 16	79.72	14	$0.627 \pm 0.012$		
2001 Jul 22	105.69	56	$0.402 \pm 0.019$		

Table A.1. continued.

ID	UT Date	B [m]	PA [deg]	$V \pm \sigma_V$	Additional informations
	2001 Jul 22	105.55	56	$0.405 \pm 0.019$	
	2001 Jul 22	104.73	57	$0.393 \pm 0.015$	
	2001 Jul 22	104.59	57	$0.413 \pm 0.016$	
	2001 Jul 22	101.55	61	$0.427 \pm 0.016$	
	2001 Jul 22	100.54	62	$0.438 \pm 0.014$	
	2001 Aug 22	86.22	15	$0.586 \pm 0.022$	
	2001 Aug 22	86.04	15	$0.581 \pm 0.020$	
	2001 Aug 22	85.95	15	$0.596 \pm 0.022$	
	2001 Aug 22	85.41	16	$0.586 \pm 0.026$	
	2001 Aug 22	85.29	16	$0.576 \pm 0.020$	
	2001 Aug 22	80.33	18	$0.631 \pm 0.028$	
	2001 Aug 22	79.97	18	$0.661 \pm 0.055$	
	2001 Aug 23	98.03	66	$0.456 \pm 0.011$	
	2001 Aug 27	86.28	14	$0.564 \pm 0.005$	
	2001 Aug 27	86.45	14	$0.565 \pm 0.003$	
	2001 Aug 27	86.46	15	$0.566 \pm 0.004$	

Notes. (1) [Dyck et al. \(1996\)](#); (2) spurious values, discarded from the computation.